

AD 745752

R-958-ARPA

May 1972

Analysis of the Mean Forcing Fields Simulated by the Two-Level Mintz-Arakawa Atmospheric Model

W. L. Gates

A Report prepared for

ADVANCED RESEARCH PROJECTS AGENCY

Reproduced by
NATIONAL TECHNICAL
INFORMATION SERVICE
U S Department of Commerce
Springfield VA 22151

Rand
SANTA MONICA, CA. 90406

51

This research is supported by the Advanced Research Projects Agency under Contract No. DAHC15 67 C 0141. Views or conclusions contained in this study should not be interpreted as representing the official opinion or policy of Rand or of ARPA.

ADDITIONAL FOR		
WHITE SECTION	<input checked="" type="checkbox"/>	
REF SECTION	<input type="checkbox"/>	
DATE RECEIVED		
DATE RECEIVED		
DATE RECEIVED		
DATE	DATE	DATE
A		

R-958-ARPA

May 1972

Analysis of the Mean Forcing Fields Simulated by the Two-Level Mintz-Arakawa Atmospheric Model

W. L. Gates

Details of illustrations in
this document may be better
studied on microfiche

A Report prepared for
ADVANCED RESEARCH PROJECTS AGENCY

I

Rand
SANTA MONICA, CA. 90406

Bibliographies of Selected Rand Publications

Rand maintains a number of special subject bibliographies containing abstracts of Rand publications in fields of wide current interest. The following bibliographies are available upon request:

*Aerodynamics • Arms Control • China • Civil Defense
Communication Satellites • Communication Systems
Computer Simulation • Computing Technology
Decisionmaking • Game Theory • Maintenance • Middle East
Policy Sciences • Probability • Program Budgeting
SIMSCRIPT and Its Applications • Southeast Asia
Space Technology and Planning • Statistics • Systems Analysis
USSR/East Europe • Weapon Systems Acquisition
Weather Forecasting and Control*

To obtain copies of these bibliographies, and to receive information on how to obtain copies of individual publications, write to: Publications Department, Rand, 1700 Main Street, Santa Monica, California 90406.

II

PREFACE

This Report is one of a series describing the results of numerical experiments with the two-level Mintz-Arakawa atmospheric model. These experiments are being carried out as part of the Rand/ARPA Climate Dynamics Program, whose primary concern is the analysis and validation of the circulation changes resulting from selected alterations of the model atmosphere's initial and/or boundary conditions. It is also necessary to compare the climatic simulations with observations, and the present work is an initial contribution in this direction.

Meteorological studies suggest that technologically feasible operations might trigger substantial changes in the climate over broad regions of the globe. Depending on their character, location, and scale, these changes might be both deleterious and irreversible. If a foreign power were to bring about such perturbations either overtly or covertly, either maliciously or heedlessly, the results might be seriously detrimental to the security and welfare of this country. So that the United States may react rationally and effectively to any such actions, it is essential that we have the capability to: (1) evaluate all consequences of a variety of possible actions that might modify the climate, (2) detect trends in the global circulation that presage changes in the climate, either natural or artificial, and (3) determine, if possible, means to counter potentially deleterious climatic changes. Our possession of this capability would make incautious experimentation unnecessary, and would tend to deter malicious manipulation. To this end, the Advanced Research Projects Agency initiated a study of the dynamics of climate to evaluate the effect on climate of environmental perturbations. The present Report is a technical contribution to this larger study.

Other Rand publications related to the present Report include R-877-ARPA, which presents the detailed documentation of the atmospheric model employed.

AD-740 093

SUMMARY

The global distributions of the mean January surface wind stress, the net diabatic heating rate, and the net rate of moisture addition as simulated in a 30-day integration with the two-level Mintz-Arakawa atmospheric general circulation model are presented. The latitudinal distributions of the zonal averages of these forcing fields are shown to be in reasonable agreement with the available observations. The most prominent discrepancies are evidently due to the model's simulation of excessive convective precipitation (and the associated convective latent heating) in the tropics, especially in the northern (winter) hemisphere. The zone of simulated tropical precipitation extends some 15° poleward of the observed position, and results in a corresponding distortion of the field of evaporation minus precipitation (or moisture-addition rate).

In determining the monthly mean forcing fields, the (convective) precipitation rate in particular should be accurately accumulated during the integration; the customary use of 6-hourly fields results in a sampling error as large as 25 percent for even the zonally averaged rainfall. With the exception of a small sampling error in the mean rate of absorption of solar radiation, the components of the other forcing fields are satisfactorily determined by 6-hourly data.

Preceding page blank

ACKNOWLEDGMENTS

Thanks are due Professors Yale Mintz and Akio Arakawa of the Department of Meteorology, University of California at Los Angeles, for permission to use their two-level general circulation model for the present simulation. I would also like to thank Professor Mintz for his constructive review of the present paper. Acknowledgment is due Robert Mobley and Al Nelson of Rand for their supervision of the computations and machine graphical output.

Preceding page blank

CONTENTS

PREFACE	iii
SUMMARY	v
ACKNOWLEDGMENTS	vii
Section	
1. INTRODUCTION	1
2. THE FORCING FIELDS IN THE MODEL	3
3. THE GLOBAL DISTRIBUTION OF THE SIMULATED FORCING FIELDS	5
A. The Net Frictional Force, \vec{F}	5
B. The Net Diabatic Heating Rate, \dot{H}	10
C. The Net Rate of Moisture Addition, $E - P$	13
4. THE ZONAL-AVERAGE SOURCE TERMS AND THEIR COMPARISON WITH OBSERVATION	17
A. The Surface Frictional Stress Components	17
B. The Components of the Net Heating Rate	19
C. The Components of the Moisture Balance	26
5. SUMMARY AND CONCLUSIONS	32
Appendix	
THE EFFECTS OF SAMPLING FREQUENCY ON THE ESTIMATION OF THE MEAN FORCING FIELDS	34
REFERENCES	43

Preceding page blank

1. INTRODUCTION

The two-level Mintz-Arakawa model of the atmospheric general circulation is one of the more widely known formulations used in extended numerical simulations of global weather and climate. This model is the simplest in terms of the physical variables retained, while still explicitly treating the cyclone-scale motions: it addresses the wind, geopotential, and temperature at only two tropospheric levels, and the moisture at only the lower level. In addition, only the more important elements of the heat and hydrological balance are simulated at the earth's surface. As a result of this simplicity, the two-level Mintz-Arakawa model is an economical formulation for producing a climatic simulation, requiring only 26 minutes on a 360/91 computer to simulate one day. This simplicity and economy would be irrelevant, of course, were it not also a fact that this model has proven capable of reproducing the major features of the mean atmospheric circulation. For these reasons, the two-level Mintz-Arakawa model has been adopted as the major simulation tool of Rand's research program in climate dynamics, and a comprehensive documentation of the model has been prepared (Gates, Batten, Kahle, and Nelson, 1971).

The atmosphere is driven primarily by the forcing functions representing the net heating and the net kinetic-energy dissipation. Together with the distribution of the excess evaporation over precipitation, and the boundary conditions at the surface, these source terms are ultimately responsible for the character of the mean circulation and climate. Since friction, heating, precipitation and evaporation are not specified ahead of time in this model, but are determined by the simulated circulation itself, the structure of the derived average forcing fields provides an important calibration of the modeling of the various physical processes that control the addition and removal of energy from the atmosphere. It is the purpose of this Report to present the average source terms, as simulated by the two-level model for a single January, and to compare these with the available observations.

The mean source terms considered here are the averages during a 30-day integration, corresponding to the month of January, during which the only change from the documented or reference integration (Gates et al., 1971) was a reduction of 10 percent in the incoming solar radiation subject to scattering. This integration was used for the present analysis for reasons of convenience, and no discussion of its possible physical significance is given here. The average climatic variables such as pressure, temperature, cloudiness, and wind simulated during the reference or control experiment itself are presented elsewhere (Gates, 1972).

2. THE FORCING FIELDS IN THE MODEL

The dynamics of the two-level Mintz-Arakawa model are formulated in terms of a vertical independent variable σ , which is a scaled pressure coordinate given by

$$\sigma = (p - p_T)/\pi \quad (1)$$

where p is pressure, p_T an assumed constant pressure at the tropopause (= 200 mb, the top of the model atmosphere) and $\pi = p_s - p_T$, the difference between the (variable) surface pressure p_s and p_T . In terms of this coordinate, the basic dynamical equations may be written

$$\begin{aligned} \frac{\partial}{\partial t} (\pi \vec{V}) + (\nabla \cdot \pi \vec{V}) \vec{V} + \frac{\partial}{\partial \sigma} (\pi \dot{\sigma} V) + f \vec{k} \times \pi \vec{V} \\ + \pi \nabla \phi + \sigma \pi \alpha \nabla \pi = \pi \vec{F} \end{aligned} \quad (2)$$

$$\begin{aligned} \frac{\partial}{\partial t} (\pi c_p T) + \nabla \cdot (\pi c_p T \vec{V}) + \frac{\partial}{\partial \sigma} (\pi c_p \dot{\sigma} T) \\ - \pi \alpha (\sigma \frac{\partial \pi}{\partial t} + \sigma \vec{V} \cdot \nabla \pi + \pi \dot{\sigma}) = \pi \dot{H} \end{aligned} \quad (3)$$

$$\frac{\partial}{\partial t} (\pi q) + \nabla \cdot (\pi q \vec{V}) + \frac{\partial}{\partial \sigma} (\pi q \dot{\sigma}) = \pi \dot{Q} \quad (4)$$

$$\frac{\partial \pi}{\partial t} + \nabla \cdot (\pi \vec{V}) + \frac{\partial}{\partial \sigma} (\pi \dot{\sigma}) = 0 \quad (5)$$

Here Eq. (2) is the vector equation of horizontal motion, Eq. (3) is the thermodynamic energy equation, and Eqs. (4) and (5) are the continuity equations for moisture and mass, respectively. Together with the equations of state ($\alpha = RT/p$) and hydrostatic balance ($\partial \phi / \partial \sigma + \pi \alpha = 0$), these are the so-called "primitive" equations of the model, expressed in terms of the horizontal vector velocity \vec{V} , the temperature T ,

the specific volume α , the mixing ratio q , and the geopotential ϕ , with the remaining symbols having their usual meanings. Of principal concern here are the forcing terms on the right-hand sides of Eqs. (2), (3), and (4), expressed in terms of \vec{F} (the horizontal frictional force per unit mass), \dot{H} (the diabatic heating rate per unit mass), and \dot{Q} (the rate of moisture addition per unit mass).

The boundary conditions accompanying this system are: $\dot{\sigma} (= d\sigma/dt) = 0$ at both $\sigma = 0$ and $\sigma = 1$, $\phi = gz_g$ at the earth's surface, where z_g is the ground elevation ($= 0$ over ocean), and the assumptions of zero net heat flux between the atmosphere and an underlying land surface and of a prescribed temperature for an underlying ocean surface. Also prescribed in the model are the locations of sea ice and of ice-covered land, where the surface temperature is not allowed to rise above 0°C .

3. THE GLOBAL DISTRIBUTION OF THE SIMULATED FORCING FIELDS

A. THE NET FRICTIONAL FORCE, $\vec{\tau}$

In the application of Eq. (2) at the discrete model levels $\sigma = 1/4$ (level 1) and $\sigma = 3/4$ (level 3), the frictional force per unit mass is given by

$$\vec{F}_1 = -\nu \left(\frac{\partial \vec{V}}{\partial z} \right)_2 \frac{2g}{\pi} \quad (6)$$

$$\vec{F}_3 = -\vec{F}_1 - C_D \rho_4 \vec{V}_s (|\vec{V}_s| + G) \frac{2g}{\pi} \quad (7)$$

Here \vec{F}_1 is an internal frictional force at level 1 proportional to the vertical stress, and hence proportional to the vertical shear $(\partial \vec{V} / \partial z)_2$ at level 2 ($\sigma = 1/2$), with ν an empirical coefficient ($= 0.44 \text{ mb sec}$), z the vertical geometric height, and the factor $2g/\pi$ the reciprocal of the mass per unit horizontal area in the upper and lower model layers. The frictional force \vec{F}_3 at the lower level 3 consists of a component equal and opposite to \vec{F}_1 and a component representing the frictional force at the surface. Hence the net frictional force $\vec{\tau}$ on an atmospheric column in the model is given by

$$\vec{\tau} = \vec{F}_1 + \vec{F}_3 = -C_D \rho_4 \vec{V}_s (|\vec{V}_s| + G) \frac{2g}{\pi} \quad (8)$$

where C_D is the surface drag coefficient, ρ_4 the surface air density, \vec{V}_s a measure of the surface wind [$= 0.7 \vec{V}_4$, where $\vec{V}_4 (= \frac{3}{2} \vec{V}_3 - \frac{1}{2} \vec{V}_1)$ is the extrapolated surface wind], and G an empirical correction for gustiness ($= 2.0 \text{ m sec}^{-1}$).

The force $\vec{\tau}$ given by Eq. (8) thus represents the surface skin friction, or alternatively, the force $-\vec{\tau}$ represents the drag of the earth on the atmosphere. The zonal and meridional components of the surface wind stress $\vec{\tau}_w \equiv -\vec{\tau}$ are given, respectively, by

$$\tau_w^\lambda = C_D \rho_4 u_s (|\vec{v}_s| + G) \frac{2g}{\pi} \quad (9)$$

$$\tau_w^\varphi = C_D \rho_4 v_s (|\vec{v}_s| + G) \frac{2g}{\pi} \quad (10)$$

where $u_s = a \cos \varphi d\lambda/dt$ is the zonal surface wind component and $v_s = a d\varphi/dt$ is the meridional surface wind component, with φ the latitude and λ the longitude on a spherical earth of radius a .

In the model, the drag coefficient C_D is given by the empirical expressions

over ocean:

$$C_D = 0.0025 \quad \text{or} \quad (0.0010 + 0.00007 |\vec{v}_s| \text{ m}^{-1} \text{ sec})$$

whichever is smaller (11)

over land or ice:

$$C_D = 0.0020 + 0.0000012 z_s \text{ m}^{-1} \quad (12)$$

Thus the surface drag is velocity dependent over the oceans, and varies between 0.001 and 0.0025. Over land (or ice) the drag depends only on the surface elevation, and varies between 0.002 over lowlands to about 0.007 over the highest mountains. For further details, see Gates et al. (1971).

The global distribution of the average zonal surface stress τ_w^λ obtained from the January simulation is given in Fig. 1, which clearly shows the presence of the mean surface midlatitude westerlies and the mean easterlies of lower latitudes in both the winter and summer hemispheres. These stresses may be compared with those for December-January-February given by Hellerman (1967); the most systematic differences are over the North Pacific ocean, where the maximum westerly and easterly stresses are simulated about 15° latitude north of their observed positions and are approximately 50 percent too strong. Over the remaining oceans, both the stress pattern and magnitude are

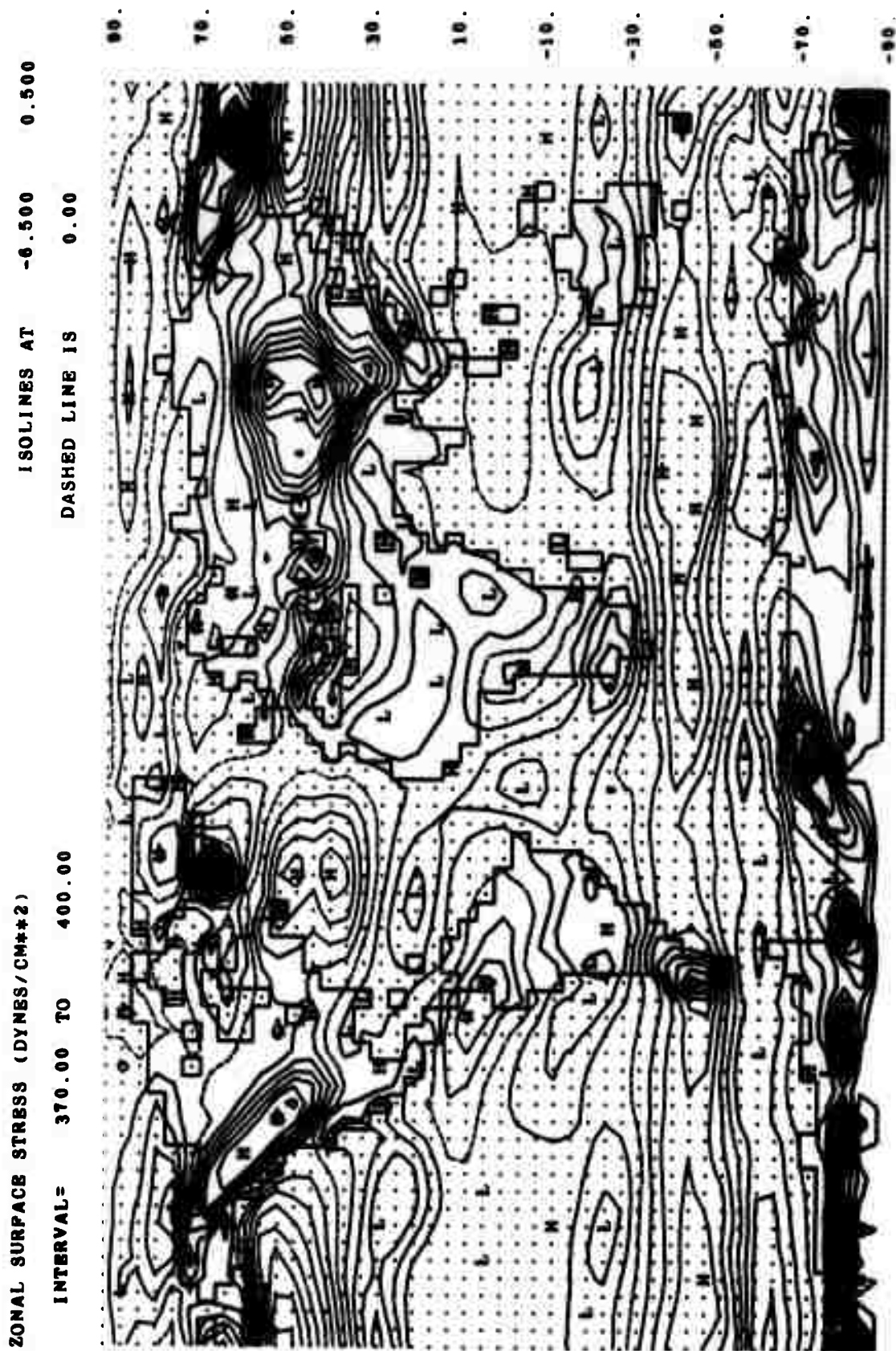


Fig. 1 -- The average zonal surface wind stress τ_λ in a 30-day January simulation with the two-level Mintz-Arakawa model. The 5° -longitude, 4° -latitude grid is shown over the oceans, with latitude given on the right. The symbols H and L denote the locations of local (relative) maxima and minima. The isolines are at 0.5 dyne cm^{-2} intervals, with the (dashed) 0 isoline separating positive (eastward) components from negative (westward) components.

in reasonably good agreement with Hellerman's data. Since Hellerman used a quadratic stress formulation similar to Eq. (9) to determine the stress from observed wind-rose data, this agreement reflects the general fidelity of at least the pattern of the simulated surface wind field. We may also note that the oceanic drag coefficient, Eq. (11), assumes approximately the same values as the coefficient used by Hellerman.

Over the continents we find the same general latitudinal dependence of the simulated zonal stress (Fig. 1) as over the oceans, but here the height dependence of the drag coefficient, Eq. (12), has produced local maxima of the stress over the Rocky, Andes, and Himalay mountains, as well as systematically increasing the stress over Greenland and Antarctica. The fidelity of these continental stress distributions over land is unknown in the absence of suitable observations, although the height dependence of C_D in Eq. (12) was taken from the drag coefficients suggested by Cressman (1960).

The corresponding distribution of the average meridional surface stress τ_w^φ obtained from the January simulation is shown in Fig. 2. Here the agreement over the oceans with the data of Hellerman (1967) is only fair; the northward stress over the northeastern North Pacific and Atlantic oceans is approximately twice the strength of that observed, while the observed broad band of southward stress in the northern hemisphere subtropical oceans is not well simulated in the model integration. In the southern hemisphere the maxima of northward stress just west of South America, Africa, and Australia at about 20°S to 30°S correspond well with observation. Over the continents, the influence of topography is again noticeable in the presence of meridional stress maxima over the Rockies, Andes, and Himalayas, as well as over portions of Greenland and Antarctica. These average patterns of meridional stress reflect the standing components of the mean meridional circulation, which in general consists in the northern hemisphere of a southward flow over the relatively cold continents with compensating northward flow over the intermediate warmer oceans. In the southern hemisphere the summer (January) meridional circulation is dominated by the subtropical oceanic anticyclones.

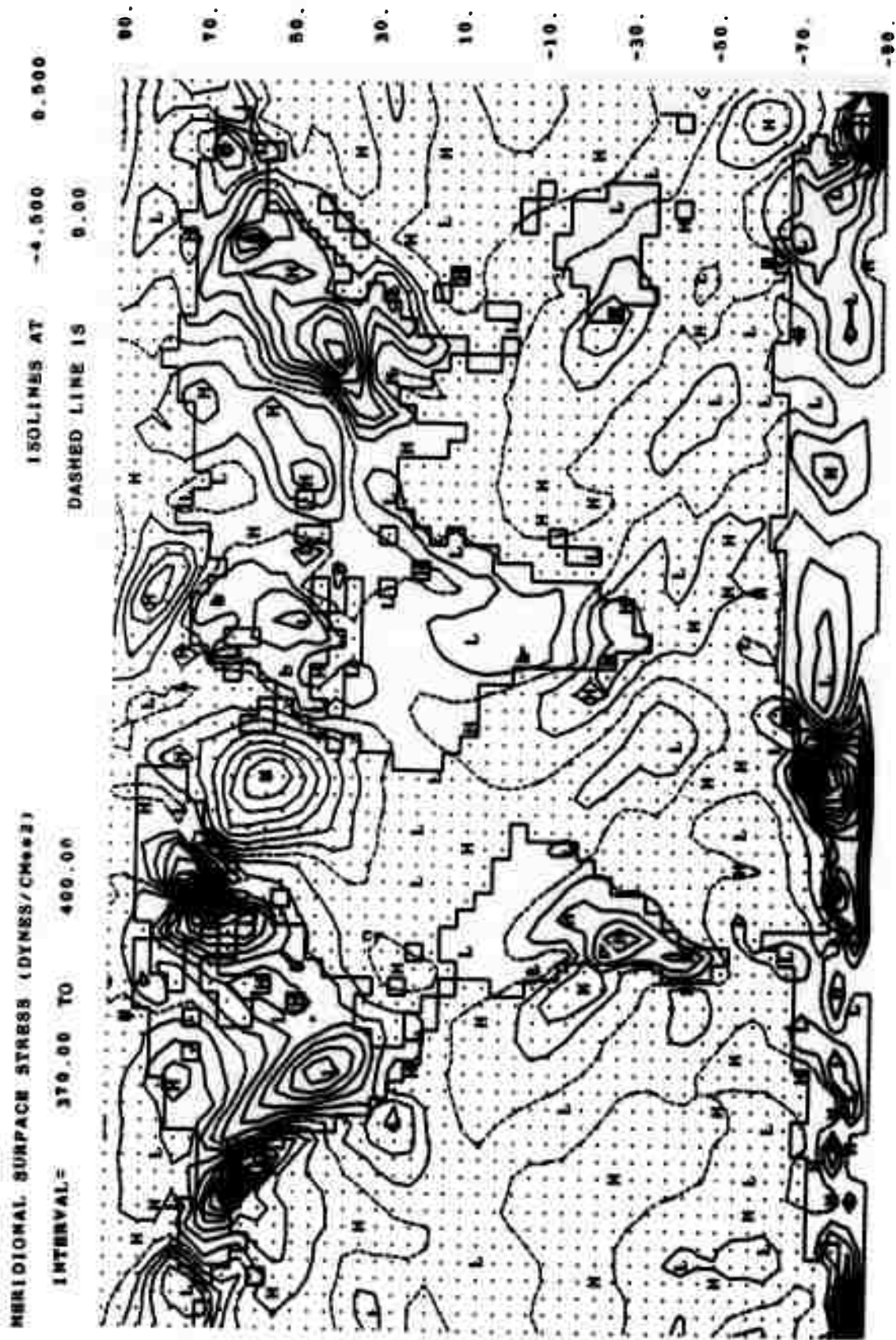


Fig. 2 -- Same as Fig. 1, except for the average meridional surface wind stress τ_w^0 , with the positive components directed northward.

Although it is the stress $\vec{\tau} = \vec{F}$ which serves as a momentum source (or sink) in the model's equation of motion (2), the frictional dissipation of kinetic energy is given by $\vec{V} \cdot \vec{F}$. This includes dissipation at levels 1 and 3, with the latter having a component dependent upon the surface wind \vec{V}_s through Eq. (7). Although it is thus not relevant to the model's energy budget (to be considered later), the surface dissipation $\vec{V}_s \cdot \vec{\tau}_s$ alone, however, has a global mean of 1.4 watts m^{-2} in the present simulation, which compares well with the value 1.5 watts m^{-2} found for the northern hemisphere spring by Ellsaesser (1969) using data of Kung.

B. THE NET DIABATIC HEATING RATE, \dot{H}

When the thermodynamic energy equation (3) is applied at level 1 ($\sigma = 1/4$) and level 3 ($\sigma = 3/4$), the diabatic heating rates \dot{H}_1 and \dot{H}_3 are given in terms of temperature change by

$$\dot{H}_1 = (A_1 + R_2 - R_0) \frac{2g}{\pi c_p} + \Delta T_{1,CM} + \Delta T_{1,CP} \quad (13)$$

$$\dot{H}_3 = (A_3 + R_4 - R_2 + \Gamma) \frac{2g}{\pi c_p} + \Delta T_{3,CM} + \Delta T_{3,CP} + \Delta T_{3,LS} \quad (14)$$

Here A_1 and A_3 are the net short-wave radiation absorbed at levels 1 and 3, and R_0 , R_2 , and R_4 are the net upward long-wave radiation emitted from the levels 0 ($\sigma = 0$), 2 ($\sigma = 1/2$), and 4 ($\sigma = 1$), respectively. Hence $A_1 + R_2 - R_0$ represents the net radiation absorbed in the upper model layer (identified with level 1), and $A_3 + R_4 - R_2$ is the net radiation absorbed in the lower layer (identified with level 3). The factor $2g/\pi c_p$ converts the heating rates to the equivalent rate of change of temperature. The term Γ represents the upward flux of sensible heat from the earth's surface, and is given by

$$\Gamma = C_D \rho_4 c_p (|\vec{V}_s| + G)(T_g - T_4) \quad (15)$$

where T_g is the ground (or ocean surface) temperature, T_4 is the surface air temperature, and the other terms are as in Eqs. (8) to (12). The remaining terms in Eqs. (13) and (14) are the rates of temperature change due to the so-called midlevel moist convection (CM), penetrating moist convection (CP), and large-scale condensation (LS). The two forms of moist convection are parameterized at both levels of the model in terms of the vertical gradients of the total heat or static energy ($c_p T + gz + Lq$), whereas the large-scale condensation depends upon the moisture condensed as a result of supersaturation at level 3 only. Details of these parameterizations are given elsewhere (Gates et al., 1971).

The net heating rate of an atmospheric column in the model may thus be written

$$\mathcal{N} = (\dot{H}_1 + \dot{H}_3) \frac{\pi c_p}{2g} = A_1 + A_3 + R_4 - R_0 + \Gamma + C_1 + C_3 + (\text{PREC}) \frac{L\pi}{2g} \quad (16)$$

where $C_1 = (\Delta T_{1,CM} + \Delta T_{1,CP}) \pi c_p / 2g$ is the upper-level convective heating, $C_3 = (\Delta T_{3,CM} + \Delta T_{3,CP}) \pi c_p / 2g$ is the lower-level convective heating, PREC is the large-scale condensation rate, and L is the latent heat of condensation.

The global distribution of the average net heating \mathcal{N} obtained from the 30-day January simulation is shown in Fig. 3. We note that over the continents of the northern hemisphere there is virtually no average net heating of the atmosphere. This may be influenced by the assumed lower boundary condition of zero net heat flux at the earth's bare-land or ice-covered surfaces, i.e.,

$$R_4 + \Gamma + H_E - S_g - I = 0 \quad (17)$$

where H_E is the flux of latent heat due to surface evaporation, S_g is the short-wave radiation absorbed at the land or ice surface, and I is the upward heat flux by conduction through sea ice. This equilibrium is in fact used to determine the appropriate ground temperature,

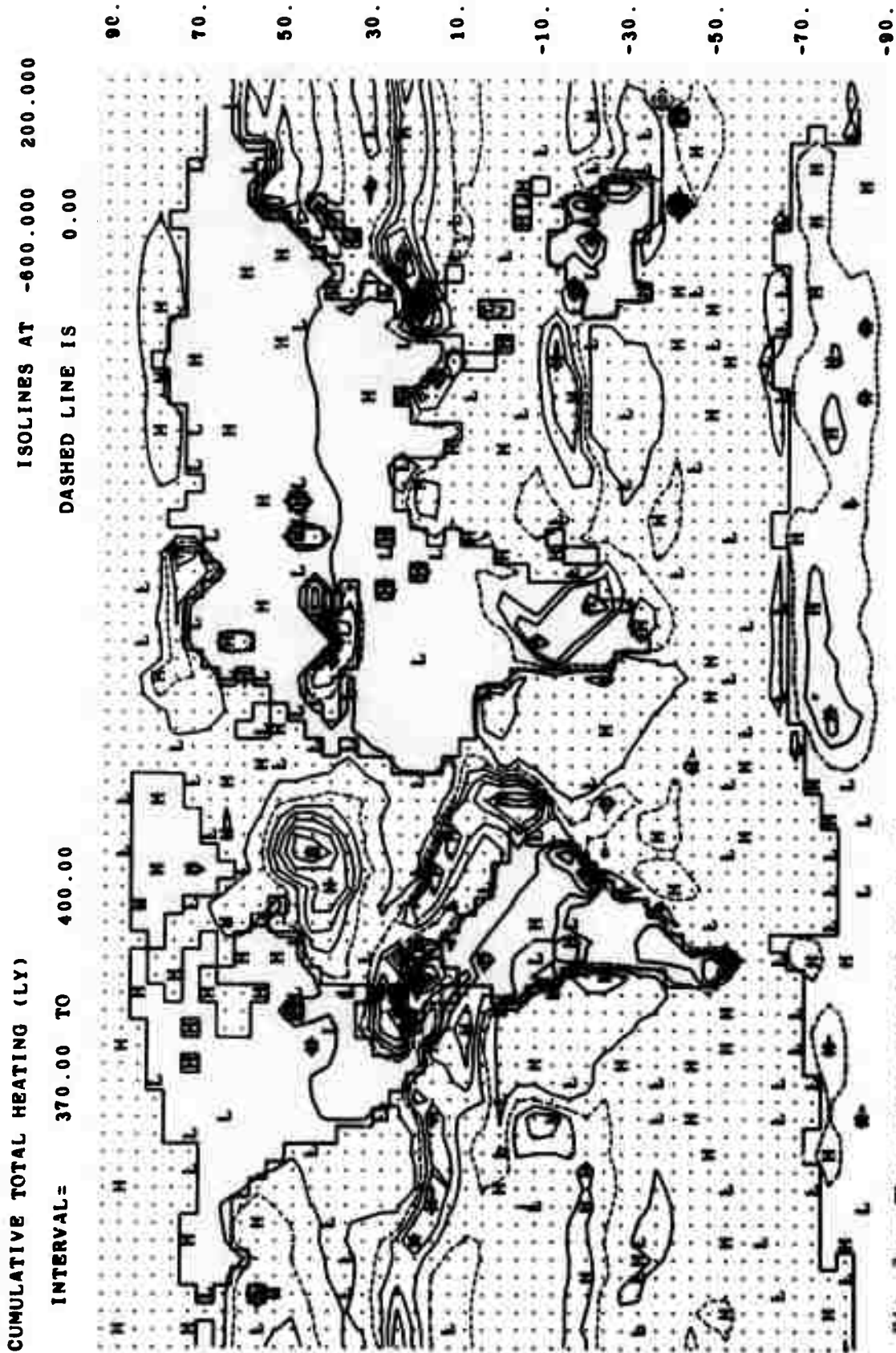


Fig. 3 -- The average net diabatic heating rate of the atmosphere in a January simulation. The isolines are at 200 ly day⁻¹ intervals, with the 0 isoline dashed (see also Fig. 1).

T_g , upon which the terms R_4 , Γ , and I depend. Thus, over land, the sensible and latent heat fluxes are used in effect to balance the surface heat budget, whereas over the oceans, where the surface temperature is held constant, the condition (17) does not apply. This results in an average net atmospheric heating where the prescribed sea-surface temperature is higher than the simulated air temperature, a condition that occurs over much of the world's oceans, as may be seen in Fig. 3. This is particularly marked in the western portions of the North Atlantic and North Pacific oceans, where the net heating exceeds 1000 ly day^{-1} . Over most of the southern-hemisphere oceans the average net heating rate is negative and of the order of -100 ly day^{-1} , with relatively weak gradients.

The dominant influence on the pattern of net heating in Fig. 3 is the distribution of the simulated convective condensation heating, C_1 and C_3 . Because these terms depend, in part, upon the air-sea temperature difference and on the available moisture in the air, it is not surprising that the net heating bears a resemblance to the distributions of both the sensible heat flux and the surface evaporation (as discussed below). It is clear from these data that the oceans exert an important controlling influence on the model atmosphere's net heat balance, and hence on the simulated mean circulation.

C. THE NET RATE OF MOISTURE ADDITION, $E - P$

When the moisture continuity equation (4) is applied at level 3 in the model, the moisture-source term \dot{Q} is given by the difference between surface evaporation and total precipitation, since it is assumed that all of the atmospheric moisture is carried at this single level. Thus

$$\dot{Q} = \dot{Q}_3 = E - P \quad (18)$$

where the surface evaporation E is given by

$$E = C_D \rho_4 \rho_w^{-1} (|\vec{V}_s| + G) (q_g - q_4) \quad (19)$$

where ρ_w is the density of water, q_a is the mixing ratio of the air just above the ground, and q_g is a mixing ratio for the ground surface itself (which includes a measure of ground wetness; see Gates et al., 1971, for details). The total precipitation, P , is assumed equal to the total condensation, and consists of the moisture released by both the large-scale and convective processes. Thus, we may write

$$P = P_{LS} + P_C \quad (20)$$

where the large-scale precipitation (or condensation) rate is given by

$$P_{LS} = (\text{PREC}) \frac{\pi}{2g\rho_w} \quad (21)$$

and the convective precipitation (or condensation) rate is given by

$$P_C = \frac{C_1 + C_3}{L\rho_w} \quad (22)$$

where PREC , C_1 , and C_3 are as in Eq. (16) and ρ_w is the density of water.

In terms of the moisture released and the consequent temperature change, we may write

$$\text{PREC} = \Delta q_{3,LS} = \Delta T_{3,LS} \left(\frac{c_p}{L} \right) \quad (23)$$

$$\begin{aligned} C_1 + C_3 &= (\Delta q_{3,CM} + \Delta q_{3,CP}) \frac{\pi L}{2g} \\ &= (\Delta T_{1,CM} + \Delta T_{1,CP} + \Delta T_{3,CM} + \Delta T_{3,CP}) \frac{\pi c_p}{2g} \end{aligned} \quad (24)$$

The moisture temporarily stored in the air as cloud is not considered in the present model, although measures of ground wetness and runoff

are included. We may also note that all precipitation is assumed to fall as rain; snow cover is prescribed (as a function of latitude) only for the purpose of determining the surface albedo.

The global distribution of the average net rate of moisture addition $\dot{Q} = E - P$ obtained from the 30-day simulation is shown in Fig. 4. This field reflects the presence of the lower-latitude precipitation maxima over the oceans (principally convective precipitation), and to this extent bears an inverse resemblance to the distribution of the average net heating rate in Fig. 3. In the subtropics, the relatively high evaporation over the oceans is the dominant moisture source, while in the higher latitudes the large-scale precipitation serves as the principal moisture sink. Over the North Pacific and North Atlantic oceans, this distribution is in broad agreement with that derived from observations for the northern winter by Jacobs (1951), although his maxima are only about half those simulated here. Over the continents in the winter hemisphere there is apparently little net contribution to the moisture balance. In the simulation, as in nature, the oceans provide most of the moisture, and receive the bulk of the precipitation in return.

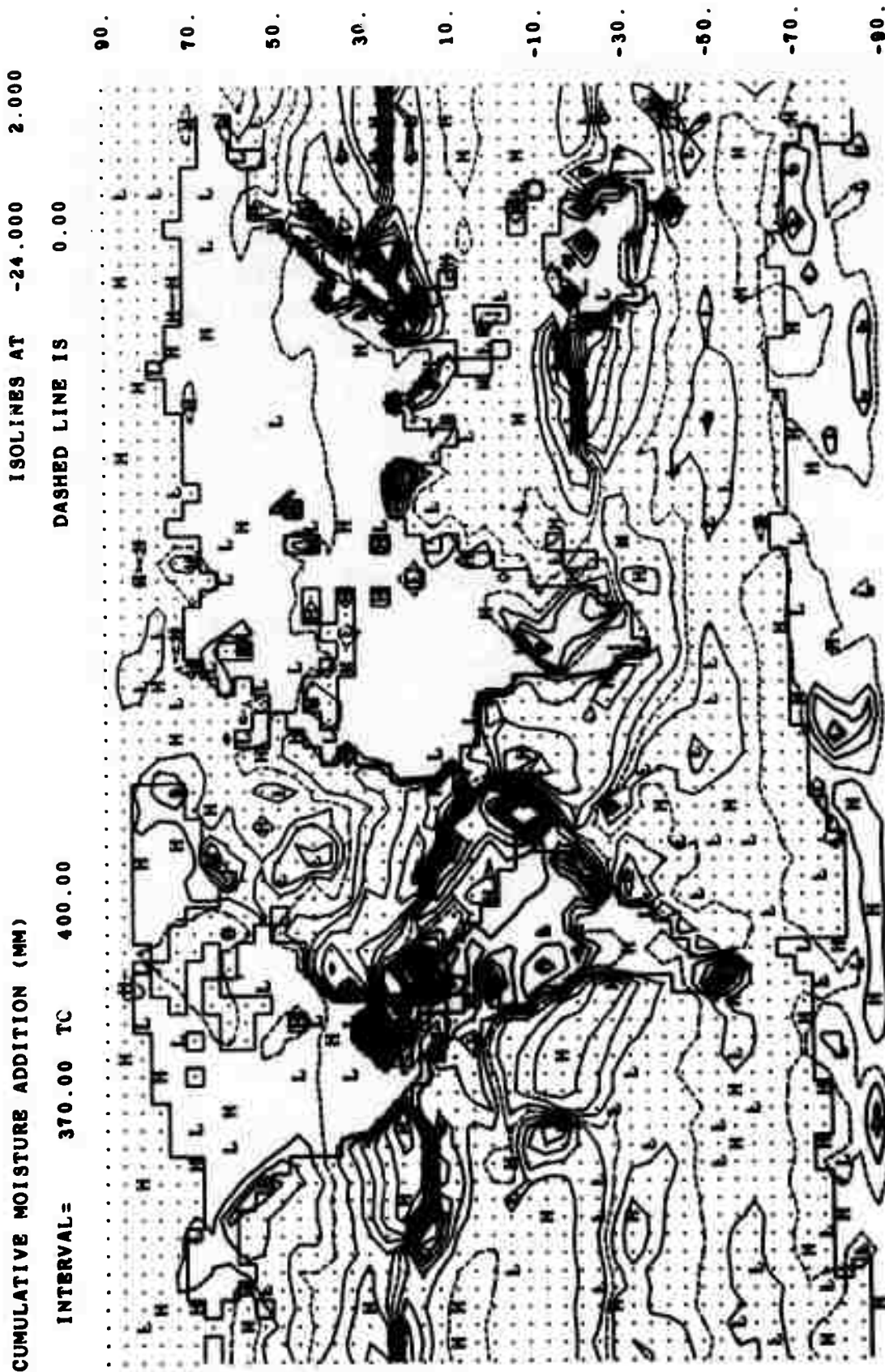


Fig. 4 -- The average net rate of moisture addition (E - P) in a January simulation. The isolines are at 2 mm day⁻¹ intervals, with the 0 isoline dashed (see also Fig. 1).

4. THE ZONAL-AVERAGE SOURCE TERMS AND THEIR COMPARISON WITH OBSERVATION

The average global distributions of the net friction, heating, and moisture sources shown in Figs. 1 to 4 correspond in general with those few observational studies available. None of these quantities, however, is directly observed, and the degree of empiricism in the available data is substantial. The present simulations, moreover, are for a single January, and may therefore differ from the longer-term average behavior of the model. For these reasons a detailed analysis of the geographical distributions of \bar{F} , \bar{H} , and \bar{Q} does not seem warranted at this time. The simulated *zonal averages*, on the other hand, may be more reliable, and may usefully be compared with observations.

A. THE SURFACE FRICTIONAL STRESS COMPONENTS

The latitudinal distribution of the zonal average of the zonal stress component τ_w^λ is given in Fig. 5, as obtained from the data of Fig. 1. For comparison with the corresponding observed data for December-January-February given by Hellerman (1957), these data have been averaged only over the oceans. While the positions of the mid-latitude westerlies and subtropical easterlies are approximately correct, their strengths are overestimated by about 50 percent in the northern hemisphere. A similar error is present in the simulated zonal winds in the troposphere (Gates, 1972). Closer inspection of Fig. 5 shows that the subtropical easterlies are about 5° poleward of their observed positions in both hemispheres. This small but systematic error may be associated with the model's calculation of the subtropical latent heating at latitudes systematically poleward of the observed positions (see Figs. 6 and 10 below). Were this oceanic zonal wind stress used to drive the ocean circulation, in which the latitudinal variation of the zonal stress controls both the location and transport of the semipermanent ocean current systems, the major oceanic gyres would be reproduced in approximately their correct positions but with about 50 percent greater intensity than would be produced by use of the observed mean stress. Such systematic simulation errors of the

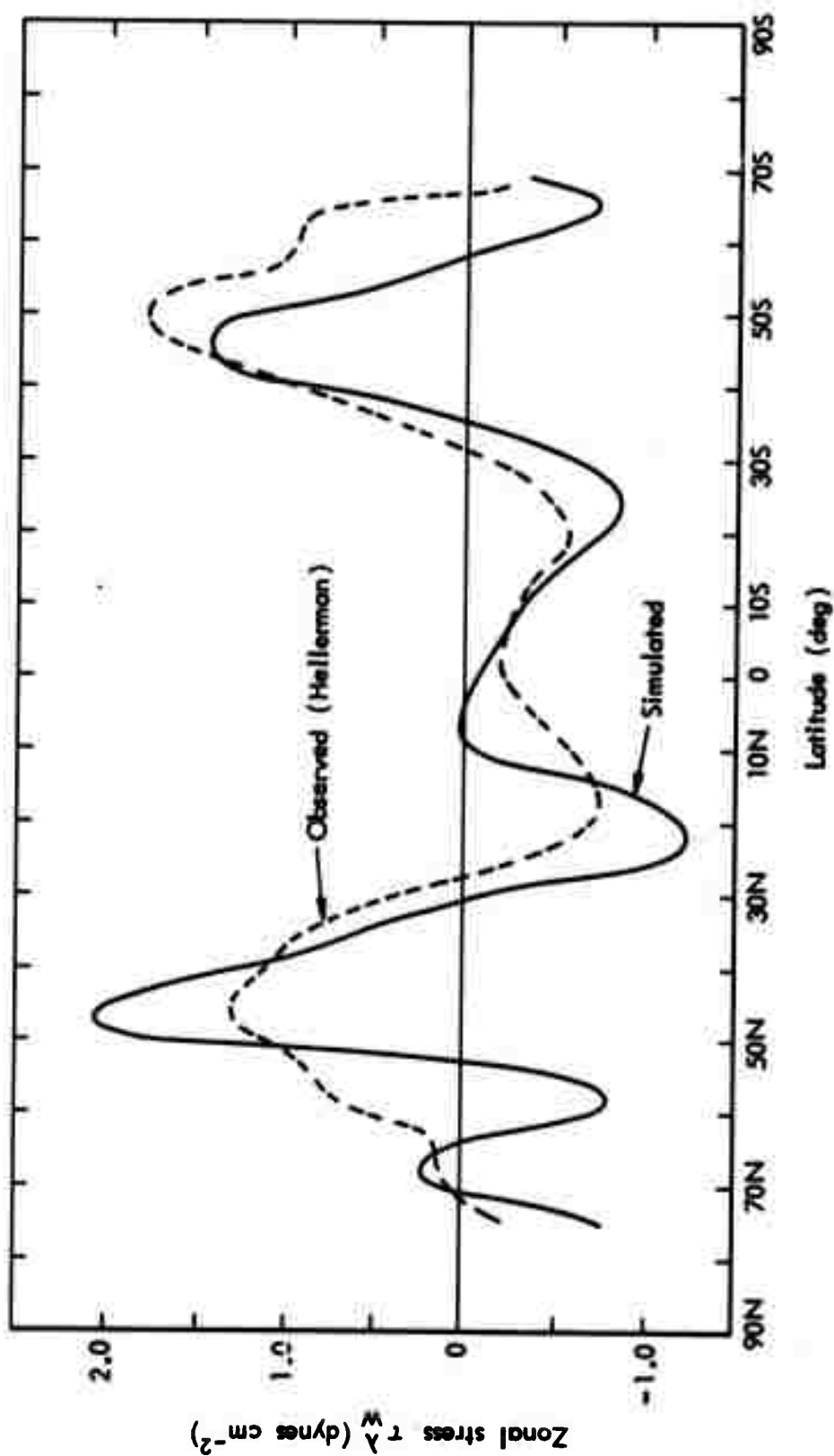


Fig. 5 -- The latitudinal distribution of the zonal average of the surface zonal frictional stress simulated for January over the oceans (full lines). The observed oceanic zonal average shown by the dashed lines is from the December-January-February data of Hellerman (1967).

atmospheric model should be corrected before they are passed on to a coupled ocean circulation.

Although less familiar to oceanographers, the zonal variation of the mean meridional surface wind stress τ_w^φ of Fig. 2 could equally well drive an ocean circulation, as the effective dynamical coupling is through $\text{curl } \vec{\tau}_w$. From Fig. 2, however, we note that only over the North Atlantic would this stress significantly contribute to the (cyclonic) ocean circulation; over most of the world's oceans the zonal variation of τ_w^φ (Fig. 2) is somewhat smaller than the meridional variation of τ_w^λ (Fig. 1).

B. THE COMPONENTS OF THE NET HEATING RATE

The latitudinal distributions of the zonal average of the components of the net heating, Eq. (16), are shown in Figs. 6 to 9. The total latent heat $C_1 + C_3 + (\text{PREC})L\pi/2g$ released by the model's condensation processes is shown in Fig. 6, together with that released by the large-scale condensation alone. From the difference between these curves, the convective processes are seen to be the more important for total atmospheric heating, and completely dominate the heating rates in the lower latitudes. In the middle latitudes of both hemispheres, the convective and large-scale condensation heating make approximately equal contributions. North of about 60°N, nearly all of the simulated latent heating is the result of large-scale (rather than convective) condensation. Over the globe, the average latent heating rate is 238 ly day^{-1} , of which 201 ly day^{-1} are from convective condensation alone.

The dominance of large-scale condensation noted above probably exists in the higher latitudes of the southern hemisphere as well. The relatively large amount of convective latent heating actually simulated between 70°S and 90°S (Fig. 6) is the result of an inadvertent (and only recently discovered) error in the model's treatment of the albedo of snow and ice. This error has caused the albedo over Antarctica in particular to be underestimated by about 0.4, giving increased absorption of solar radiation at the surface. This has in turn resulted

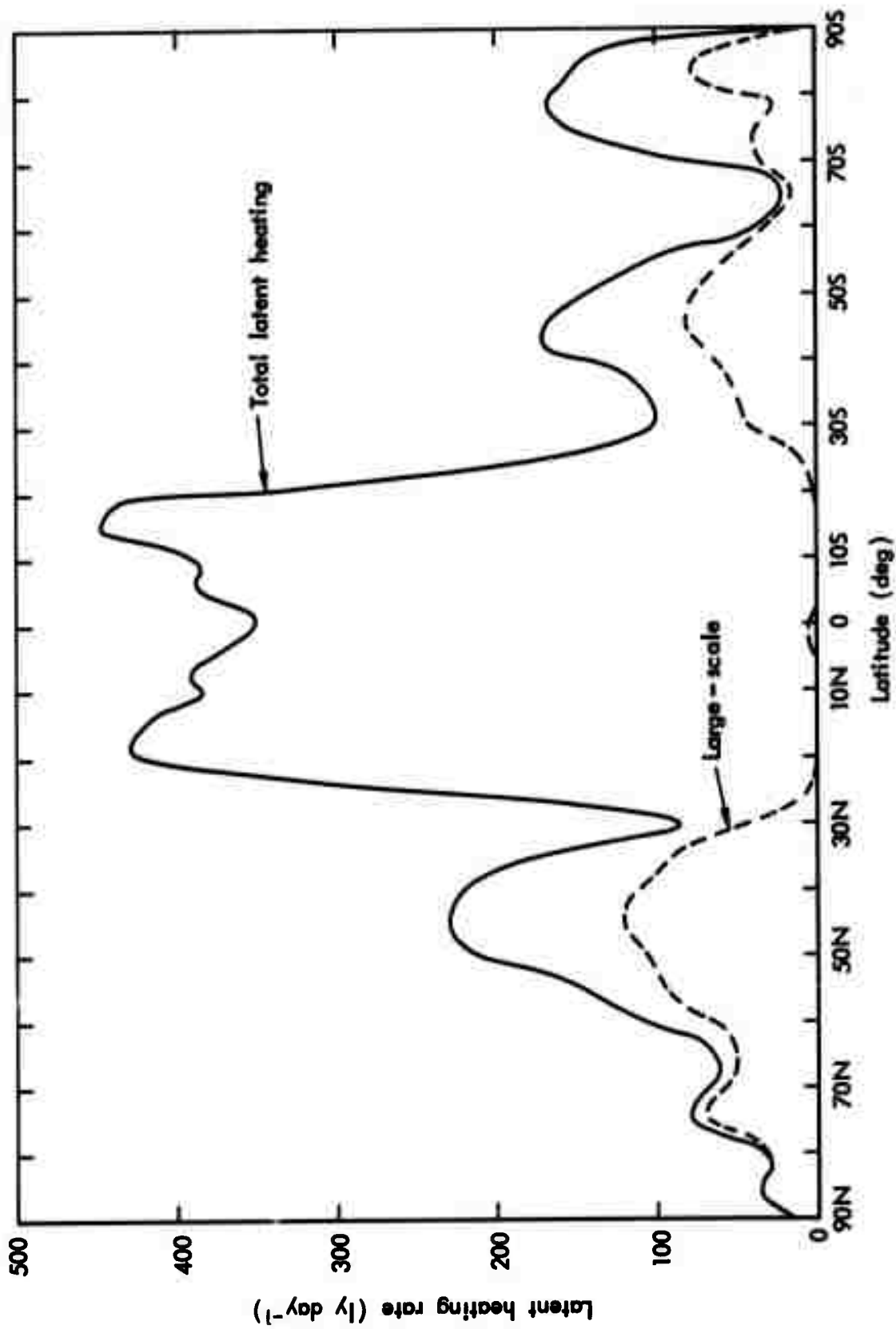


Fig. 6 -- The latitudinal distribution of the zonal average of the simulated January latent heating rate due to large-scale condensation, given by $(\text{PREC})L\pi/2g$, and the total latent heating rate due to both large-scale and convective condensation ($C_1 + C_3$) as in Eq. (16).

in anomalously high surface temperatures, from which the simulation of convection has followed by virtue of the decreased vertical stability. The results of this albedo error are also noticeable in the simulated fields of radiative heating, sensible heat flux, precipitation, and evaporation discussed below (see also Gates, 1972).

Figure 7 shows the latitudinal distribution of the net rate of short-wave (solar) radiation absorption by water vapor and clouds in the atmospheric column; in Eq. (16) this is given by $A_1 + A_3$, the sum of the net insolation absorption rate in the upper and lower model layers. The model's rate of absorption is close to, but systematically less than, the observed data given by London (1957) for the northern hemisphere winter. In the southern hemisphere, the simulated short-wave radiative heating rate is significantly greater than that given for January by Sasamori, London, and Hoyt (1971). Some of this discrepancy, especially at the higher southern latitudes, is probably due to the model's error in the albedo of ice, which permits about twice as much solar radiation to be absorbed at the surface as is observed.

Also shown in Fig. 7 is the latitudinal distribution of the net rate of long-wave radiative heating, given by $R_4 - R_0$ in Eq. (16), the difference between the long-wave emission from the surface and that from the top of the model atmosphere. Since $R_4 - R_0 < 0$, the long-wave radiation produces a net cooling of the atmospheric column. For the January conditions simulated, there is no solar radiation absorbed north of about 70°N , whereas over the remainder of the globe, both the short- and long-wave radiative heating are affected by the simulated distributions of water vapor and cloudiness. The agreement with the data of London (1957) and of Sasamori, London, and Hoyt (1971) is good north of 30°S ; south of this latitude there is a systematic underestimation of the long-wave cooling rate by about 30 percent.

The maximum cooling rate given by the total radiative heating ($A_1 + A_3 + R_4 - R_0$) occurs in the northern subtropical latitudes, and agrees reasonably well with observation. The minimum heating simulated in the higher latitudes of the southern hemisphere, however, is an exception. Here the model's ice-albedo error noted earlier may be the cause of the discrepancy south of 65°S . Over the southern oceans (40°S

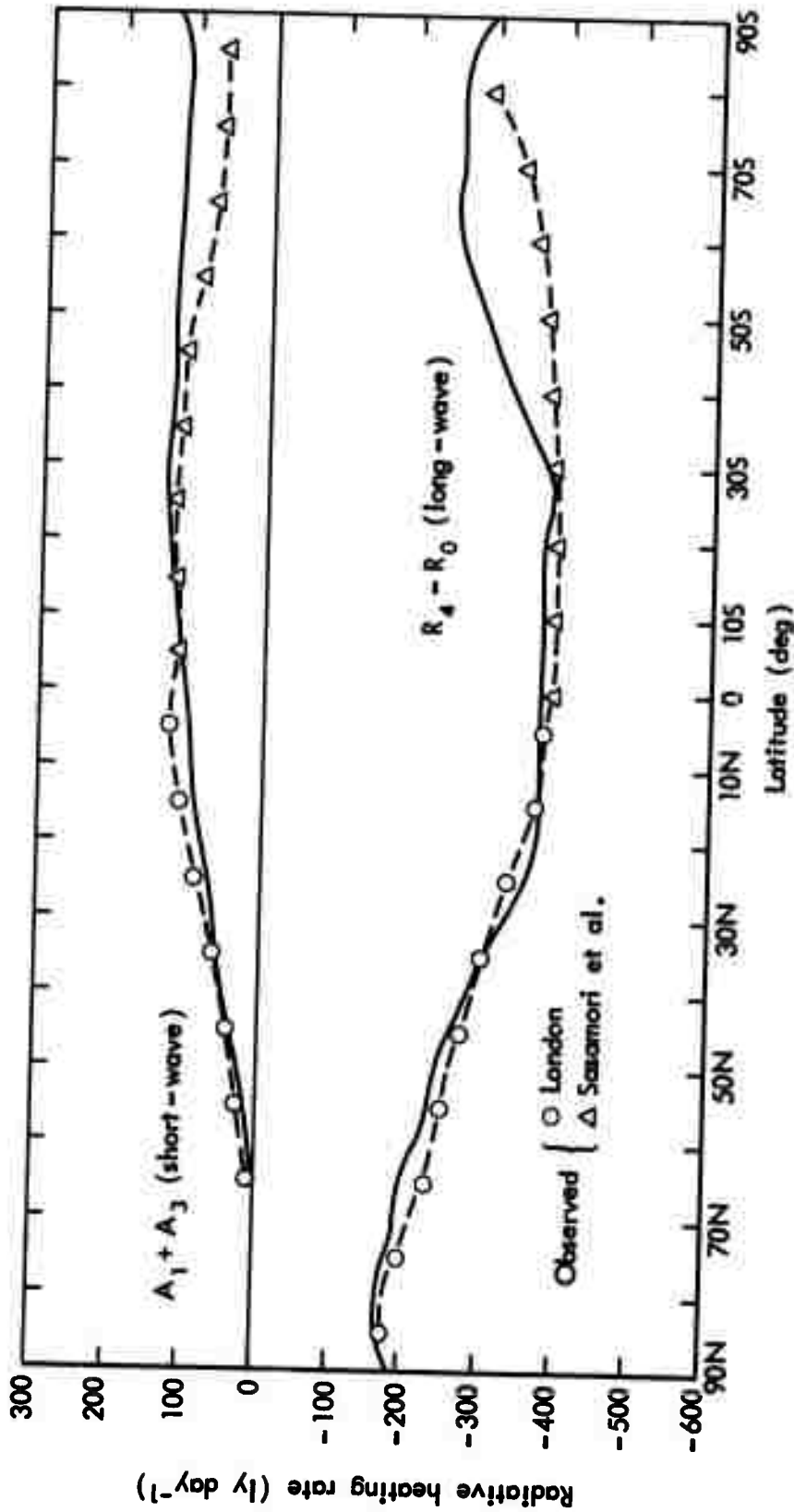


Fig. 7 -- The latitudinal distribution of the zonal average of the simulated January rate of absorption of solar radiation by water vapor and clouds, given by $A_1 + A_3$ as in Eq. (16) (upper curve), and the net rate of long-wave radiative cooling as given by $R_4 - R_0$ (lower curve). The corresponding observed data in the northern hemisphere (open circles) is from London (1957), and that in the southern hemisphere (open triangles) from Sasamori, London, and Hoyt (1971).

to 60°S), however, there are also systematic errors in the simulated surface balance that appear to be due to the model's underestimation of the cloudiness (Gates, 1972). Over the globe, the average radiational heating rate is -232 ly day^{-1} , with averages of -323 ly day^{-1} and 91 ly day^{-1} for the long-wave and short-wave heating rates, respectively.

The latitudinal distribution of the simulated zonal average heating rate Γ due to the vertical (turbulent) flux of sensible heat from the surface is given in Fig. 8. The prominent positive heat flux between approximately 20°N and 50°N is due to the large upward heat flux over the oceans off the east coasts of Asia and North America, whereas the positive flux between approximately 20°S and 40°S is due to the upward flux over the relatively warm continents of the southern (summer) hemisphere. The downward (negative) fluxes near the equator and near 60°S may be due to the relatively cool ocean surface temperatures prescribed at these latitudes, while the negative flux at high northern latitudes is due to the formation of a ground inversion ($T_g < T_4$) over the land and sea ice, in the absence of significant solar radiation in January. The global average sensible heat flux is 13 ly day^{-1} .

In comparison with the observed distribution of the zonal average sensible heat flux given by Schutz and Gates (1971), based upon data of Budyko (1963), the midlatitude maxima are reasonably well depicted (although overestimated) in the simulation. More serious is the model's replacement of the low but positive sensible heat flux in latitudes 10°N to 20°S by a downward (negative) flux. The cause of this discrepancy is the excessive heating of the air by the convective condensation, which has made the air warm enough to reverse the sign of the (usual) surface sensible heat flux. We may also note the simulation of an upward sensible heat flux south of about 70°S; this feature is likely due to the high surface temperatures over Antarctica, caused by the model's underestimation of the albedo of ice noted earlier.

Figure 9 shows the latitudinal distribution of the zonal average of the total heating rate of the model atmospheric column ($p \geq 200 \text{ mb}$),

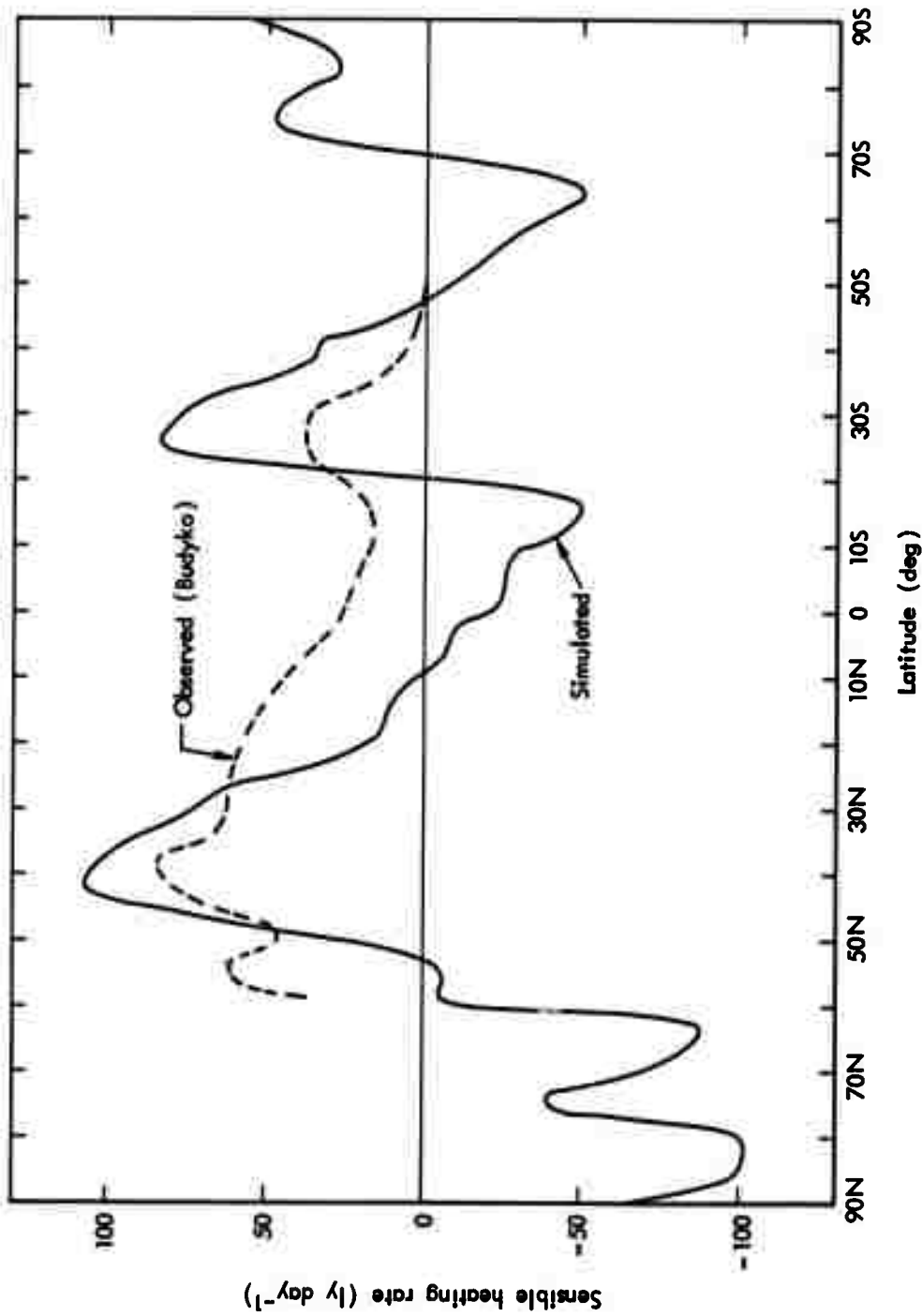


Fig. 8 -- The latitudinal distribution of the zonal average of the simulated January heat flux due to the vertical (turbulent) transfer of sensible heat, as given by Γ [Eq. (15)]. The observations (open circles) are from Schutz and Gates (1971), based on data of Budyko (1963).

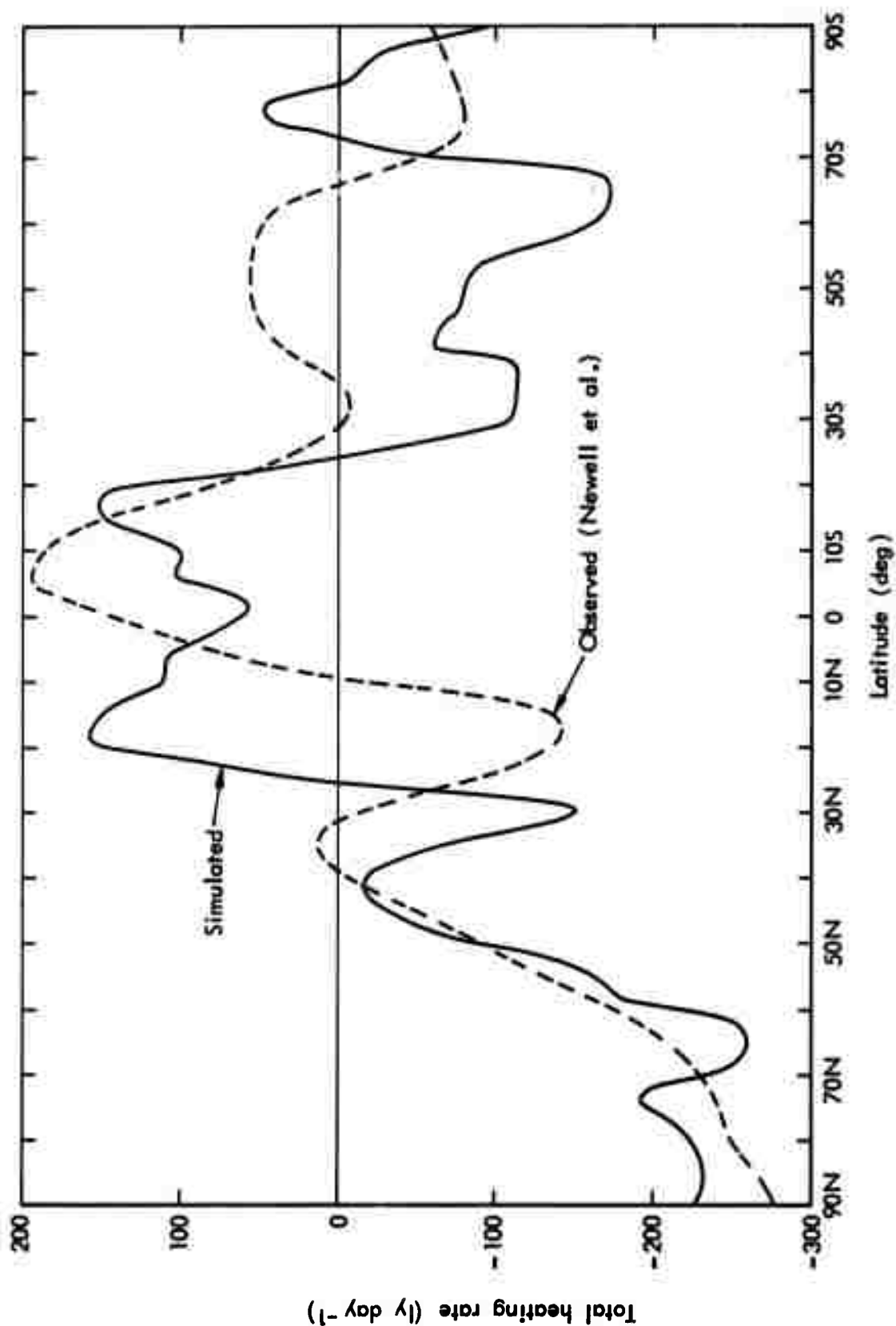


Fig. 9 -- The latitudinal distribution of the zonal average of the simulated January total (net) heating rate of the atmosphere, as given by \mathcal{H} in Eq. (16). The dashed curve is the observed total heating rate for December-January-February given by Newell et al. (1970).

as given by \bar{N} in Eq. (16); this is the sum of the distributions shown in Figs. 6, 7, and 8 (or the zonal average of the data of Fig. 3). The principal simulated January heating of the atmosphere is seen to occur between about 25°N and 25°S, and is approximately symmetric about the equator. Comparison with Fig. 6 shows that the distribution is strongly influenced by the latent heat released through convective precipitation. In comparison with the observed net heating of the atmosphere given by Newell et al. (1970), the simulation in the northern hemisphere may be considered satisfactory, except for the model's northward displacement, by some 15°, of the subtropical zone of minimum heating. In the southern hemisphere the agreement is much less satisfactory, although the simulated and observed heating curves have generally similar features. The positive total heating simulated around 70°S is due to both the excessive short-wave absorption and the excessive convective latent heating noted earlier. In the global average, the computed net heating rate is -16 ly day^{-1} ; this corresponds to a cooling of the entire atmosphere over the 30-day simulation of about 1 deg C, and is not inconsistent with the conditions of this particular experiment (See Section 1).

C. THE COMPONENTS OF THE MOISTURE BALANCE

The latitudinal distribution of the zonal average of the simulated January precipitation is shown in Fig. 10. Here we see that the total precipitation (equal to the total condensation in the model) is a reasonably accurate approximation to the observed December-January-February precipitation as given by both Lvovitch and Ovtchinnikov (1964) and by Möller (1951) in the middle and high latitudes of both hemispheres. An exception occurs over Antarctica, where the model's simulation is doubtful due to the albedo error noted earlier). Between about 30°N and 30°S, however, the observed precipitation is overestimated in the simulation by approximately 50 percent, with the tropical rainfall maxima displaced 10° to 15° toward the poles. This error is primarily responsible for the simulated global average January precipitation rate of 4.11 mm day^{-1} being so far above the observed rate of 2.94 mm day^{-1} [from the data of

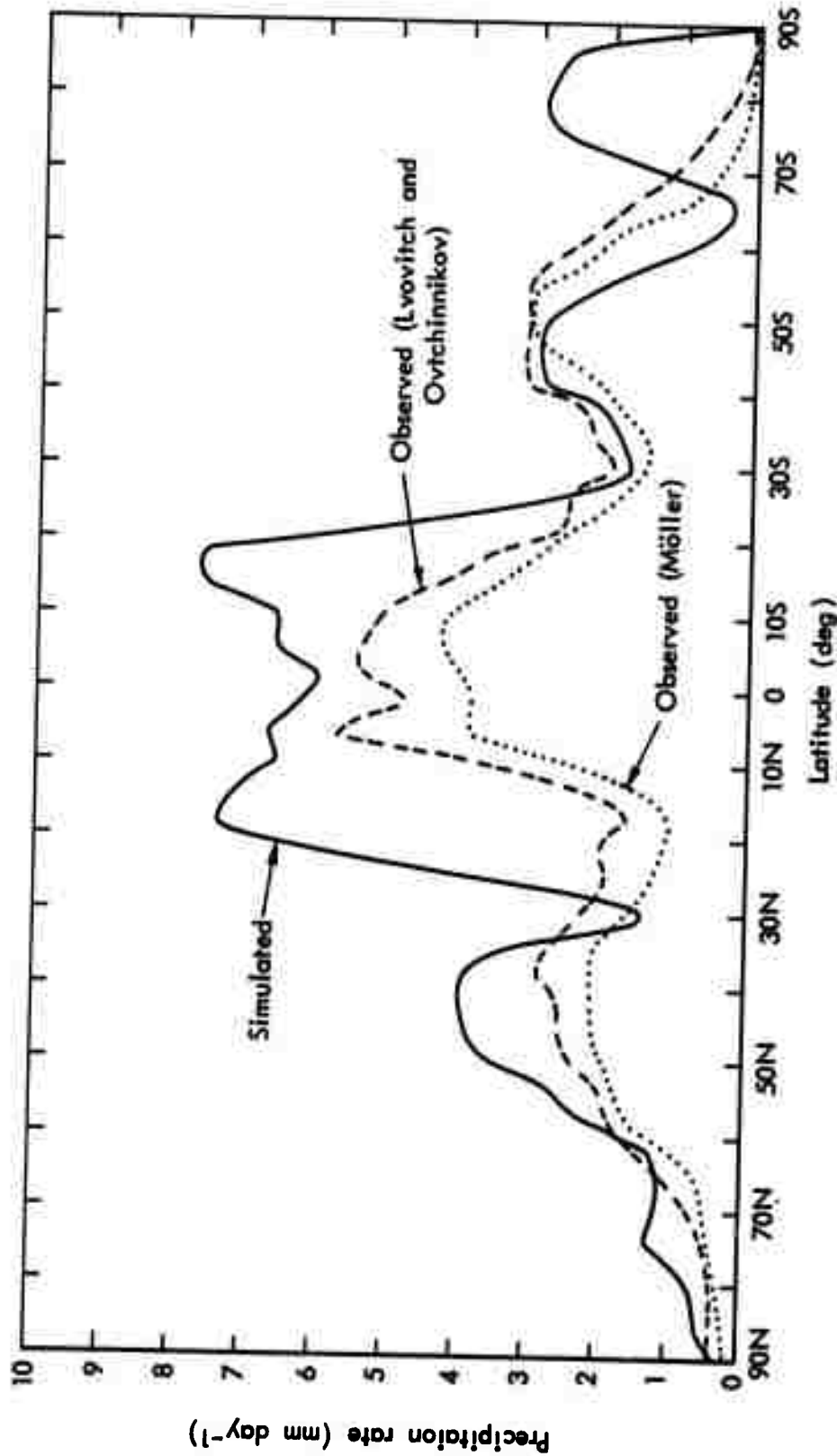


Fig. 10 -- The latitudinal distribution of the zonal average of the simulated January total precipitation rate, as given by P [Eq. (20)]. The dashed curve is the observed precipitation rate for December-January-February as given by Schutz and Gates (1971) using data of L'vovitch and Ovtchinnikov (1964), and the dotted curve is from the December-January-February precipitation data given by Möller (1951).

Lvovitch and Ovtchinnikov (1964)] or 2.20 mm day^{-1} [from the data of Möller (1951)]. Between 70°S and 90°S , the anomalously large simulated precipitation rate is due to the convection resulting from high surface temperatures, which in turn are caused by the model's inadvertent use of an albedo for ice which is only about half the correct one.

The simulated precipitation in Fig. 10 is proportional to the total latent heating in Fig. 6, with a heating rate of 100 ly day^{-1} corresponding to a precipitation (condensation) rate of approximately 1.72 mm day^{-1} . The excessive precipitation modeled in the tropics is thus seen to be due almost entirely to convective processes, just as was the total heating of Fig. 9. An improvement in the parameterization of convection could therefore be expected to aid both the precipitation and heating-rate simulations considerably.

The latitudinal distribution of the zonal average January evaporation, both as simulated and as given by Schutz and Gates (1971) based on the data of Budyko (1963), is given in Fig. 11. As with the precipitation, we see that between approximately 30°N and 30°S the simulated evaporation rate is about 50 percent greater than that observed. Like the precipitation error, this discrepancy may be mainly due to convection, with the surface evaporation attempting to moisten the atmosphere made too dry by excessive rainfall. It is known that the simulated relative humidity at level 3, for example, is only about half that observed at 800 mb between the latitudes 30°N and 20°S (Gates, 1972). Such a discrepancy would be sufficient to explain the evaporation error, since the model's mixing ratio q_4 depends primarily upon the level-3 relative humidity and the ground wetness [see Gates et al. (1971)]. The large evaporation rate simulated south of 70°S , like the precipitation (Fig. 10) and sensible heat flux (Fig. 8), is due to the excessively high surface temperatures over the Antarctic ice (Gates, 1972).

The latitudinal distribution of the zonal average of the difference $E - P$, the net rate of moisture addition to the atmospheric column, is shown in Fig. 12 as simulated for January, together with two measures of the observed distribution. The simulation may in general be considered a satisfactory approximation to observation. The sub-

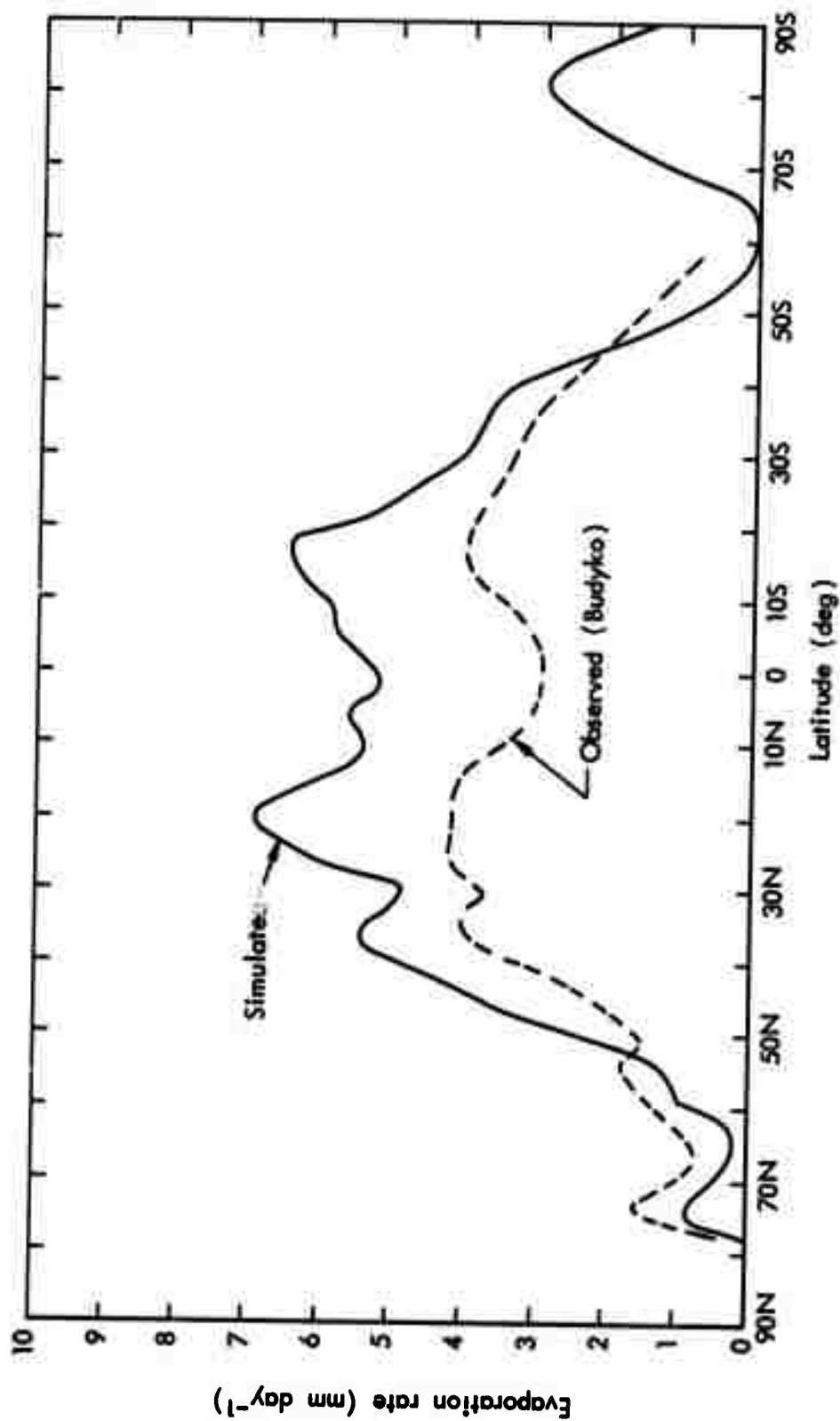


Fig. 11 -- The latitudinal distribution of the zonal average of the simulated January evaporation rate, as given by E [Eq. (19)]. The dashed curve is the observed January evaporation rate from Schutz and Gates (1971) based on data of Budyko (1963).

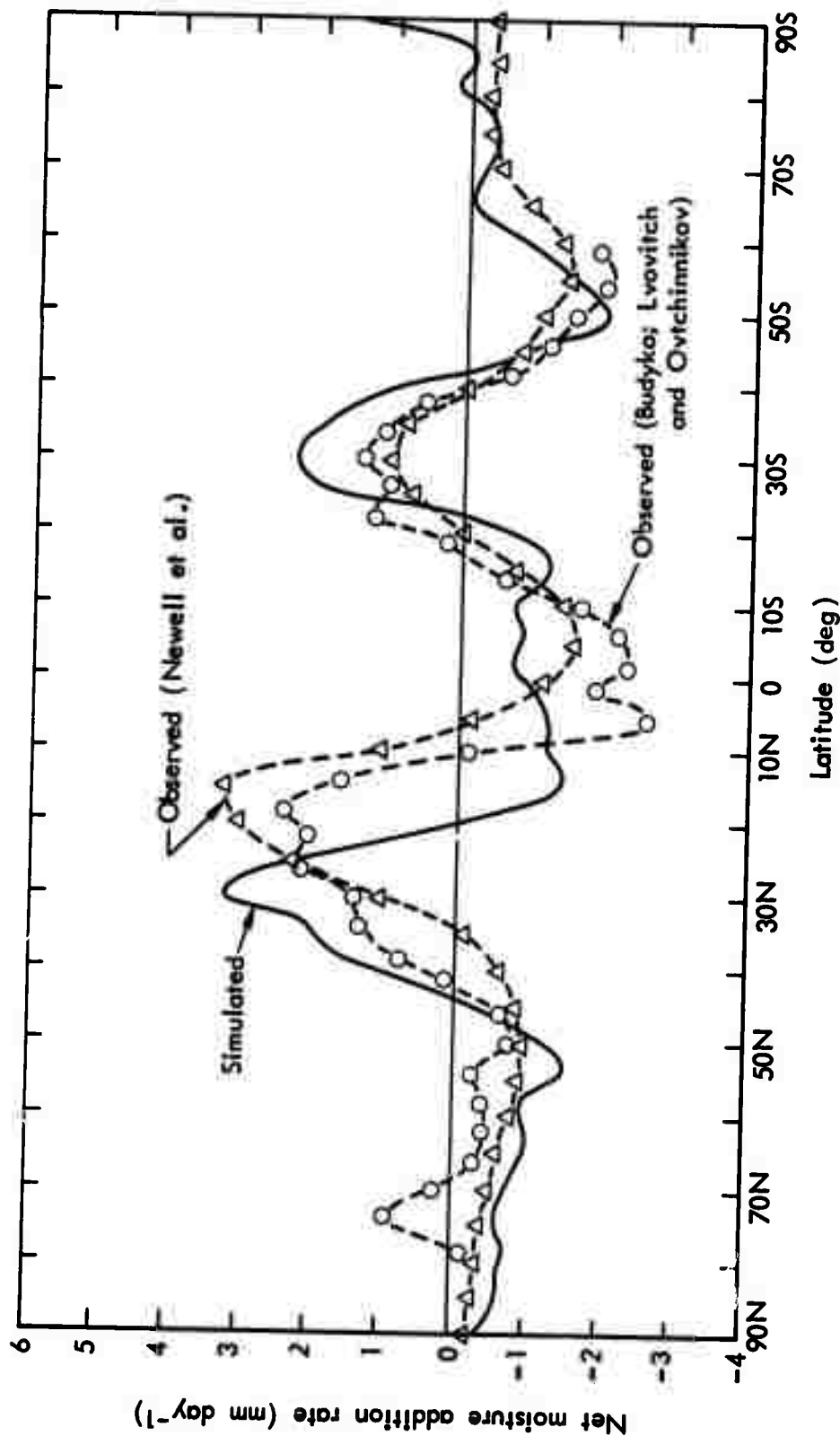


Fig. 12 -- The latitudinal distribution of the zonal average of the simulated January net moisture addition rate, E - P. The dashed curve with open triangles is the observed rate given by Newell et al. (1970) using data from various sources, whereas that with open circles is the observed distribution according to the data of Budyko (1963), as summarized by Schutz and Gates (1971), and of Lvovitch and Ovtchinnikov (1964).

tropics near 30°N are seen to be the atmosphere's primary January moisture source, with the region around 30°S a secondary source. The simulated E - P maximum in the northern hemisphere, however, is displaced some 10° north of the observed, due to the excessive precipitation simulated between 10°N and 25°N (see Fig. 10). In the equatorial region the simulated negative E - P is only about half that observed; this is due to the model's excessive evaporation in this region, as noted earlier (see Fig. 11). On the global average the January evaporation and precipitation very nearly balance when averaged over the 30-day simulation, with a net E - P of only $-0.02 \text{ mm day}^{-1}$.

5. SUMMARY AND CONCLUSIONS

From the January simulation summarized here, it has been shown that the two-level Mintz-Arakawa model is capable of depicting the average forcing or source fields for momentum, heat, and moisture with reasonable accuracy. The simulated surface stress (or net frictional force on an atmospheric column) agrees fairly well with the general pattern of observed stress derived from surface-wind observations, although the magnitude of the stress is systematically overestimated. The simulated net heating rate of an atmospheric column shows fair agreement with observation, but suffers from an excessive latent heating rate in the tropics because of the model's apparent overcalculation of convective condensation. The sensible heat flux is also in error in the tropics; here the simulated flux is in fact opposite in sign to that observed. The net long- and short-wave heating rates for the atmospheric column agree reasonably well with observation, but here too there are some systematic errors.

Although an analysis of the model's simulation of the global January climate is given elsewhere (Gates, 1972), the present simulation of the primary forcing fields \vec{F} , \dot{H} , and \dot{Q} of the system, Eqs. (2) to (4), is sufficiently accurate to lead one to expect a reasonably satisfactory simulation of the average climatic elements such as pressure, temperature, humidity, and wind. The most prominent simulation error which appears to have significantly affected the forcing fields is the model's calculation of maximum (convective) precipitation at about 20°N and 20°S, rather than at the observed locations near 5°N and 5°S. This error carries over into the net heating rate, and effectively compresses the subtropical zones poleward of their observed positions, especially in the northern (winter) hemisphere. The enhanced meridional heating gradient and the resultant baroclinicity may therefore be a cause of the excessive strength of the simulated zonal winds, and of the associated excessive strength of the midlatitude cyclones. A complete analysis of the simulated circulation's energy budget and its partitioning into mean and eddy components in both space and time is necessary to verify this conjecture, however.

A second systematic error noted here at high southern latitudes is the model's simulation of too much absorbed solar radiation, too much (convective) precipitation and evaporation, and an upward sensible heat flux. These discrepancies are believed due to an inadvertent error in the albedo of ice, and are not considered characteristic of the model itself. It may also be noted that the present results have been derived from a single 30-day January integration, and not from the average of many such January simulations. The year-to-year variations produced by the model clearly need to be examined before a definitive assessment can be made of the accuracy of the simulated climate.

APPENDIX

THE EFFECTS OF SAMPLING FREQUENCY ON THE ESTIMATION OF THE
MEAN FORCING FIELDS

The components of the average heating and moisture-addition rates discussed above have been determined from the 30-day net accumulation of the various terms, with the accumulation updated every time the components are computed in the program (every 1/2 hour). These fields have therefore been determined as accurately as they could be with the present model. For many climatological variables, however, a less frequent sampling is sufficient to determine a reliable monthly mean. In the present model simulations, a basic set of meteorological variables is normally saved on a history tape every six hours, from which the various components of the heating, for example, may be determined by reentering the appropriate portion of the program at that time. As anticipated, the six-hour sampling frequency was found to determine with sufficient accuracy the simulated January average pressure, temperature, and wind distributions (see Gates, 1972), as well as quantities involving only simple manipulations of these basic variables. It was less clear, however, that the net forcing fields for heat (\bar{N}) and moisture (\bar{Q}) would be as accurately portrayed by six-hourly sampling. For this reason the averages of these fields were determined with several sampling intervals over a selected ten-day interval of the January simulation, and the results are summarized below.

Of the components of the heating rate \bar{N} , Eq. (16), the distributions of the net long-wave radiative cooling, $R_4 - R_0$, the sensible heat flux Γ , and the latent heating due to large-scale condensation $(\text{PREC})L\pi/2g$ showed no significant differences in the cases of 1/2-hr and 6-hr sampling frequencies (480 and 40 samples, respectively, during the 10-day interval). The heating rate due to absorbed solar radiation, $A_1 + A_3$, however, displays a small but noticeable change when sampled every 6 hr rather than every 1/2 hr, as shown in Figs. A1 and A2. This error takes the form of a spurious enhancement of a 90° longitude zonal harmonic tied to the sun's local position at sampling times.

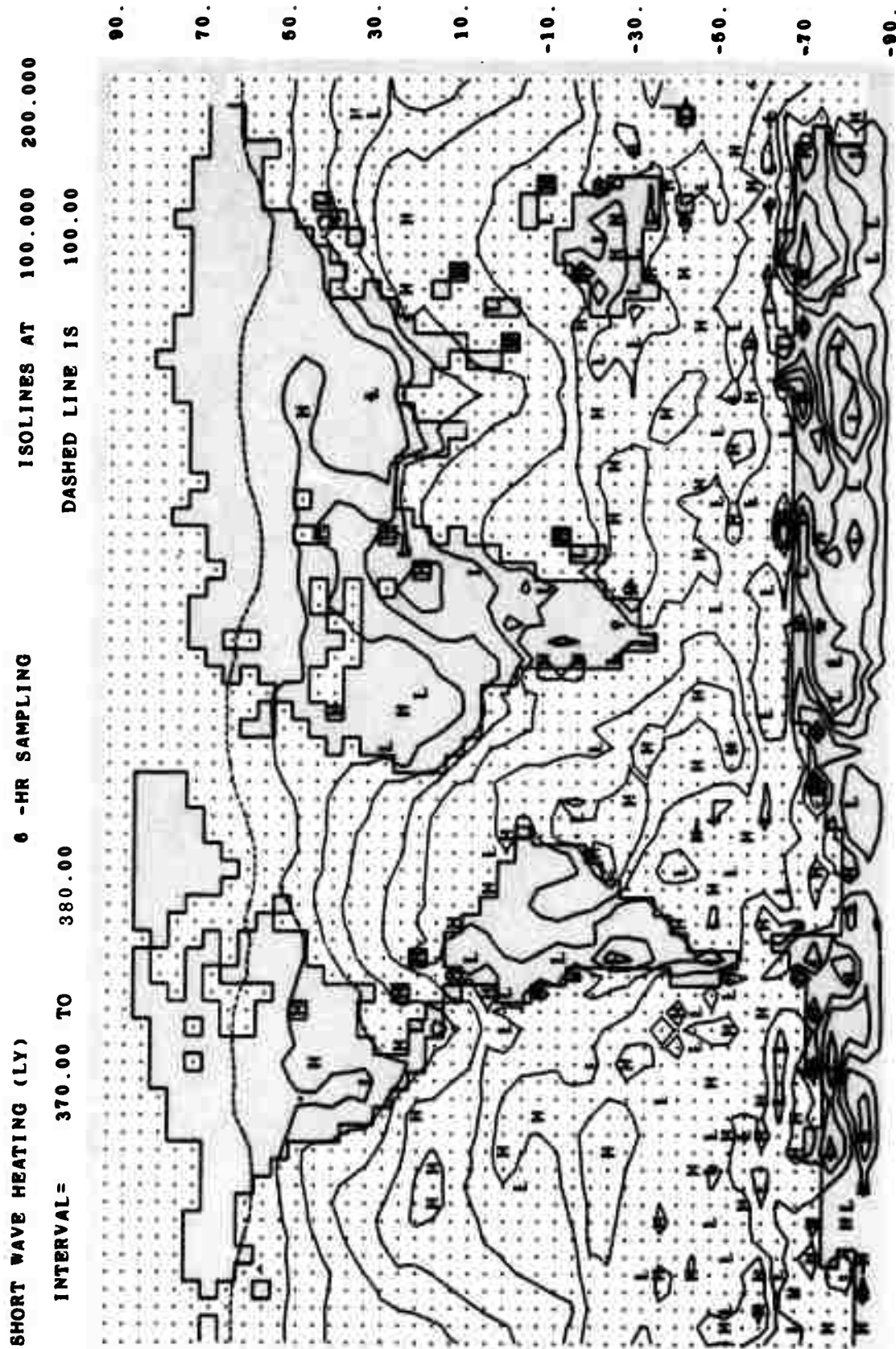


Fig. A1 -- The average rate of short-wave heating during 10 days of a January simulation, as given by sampling every 6 hr. The isolines are at 200 ly day⁻¹ intervals, with the 100 ly day⁻¹ isoline dashed (see also Fig. 1).

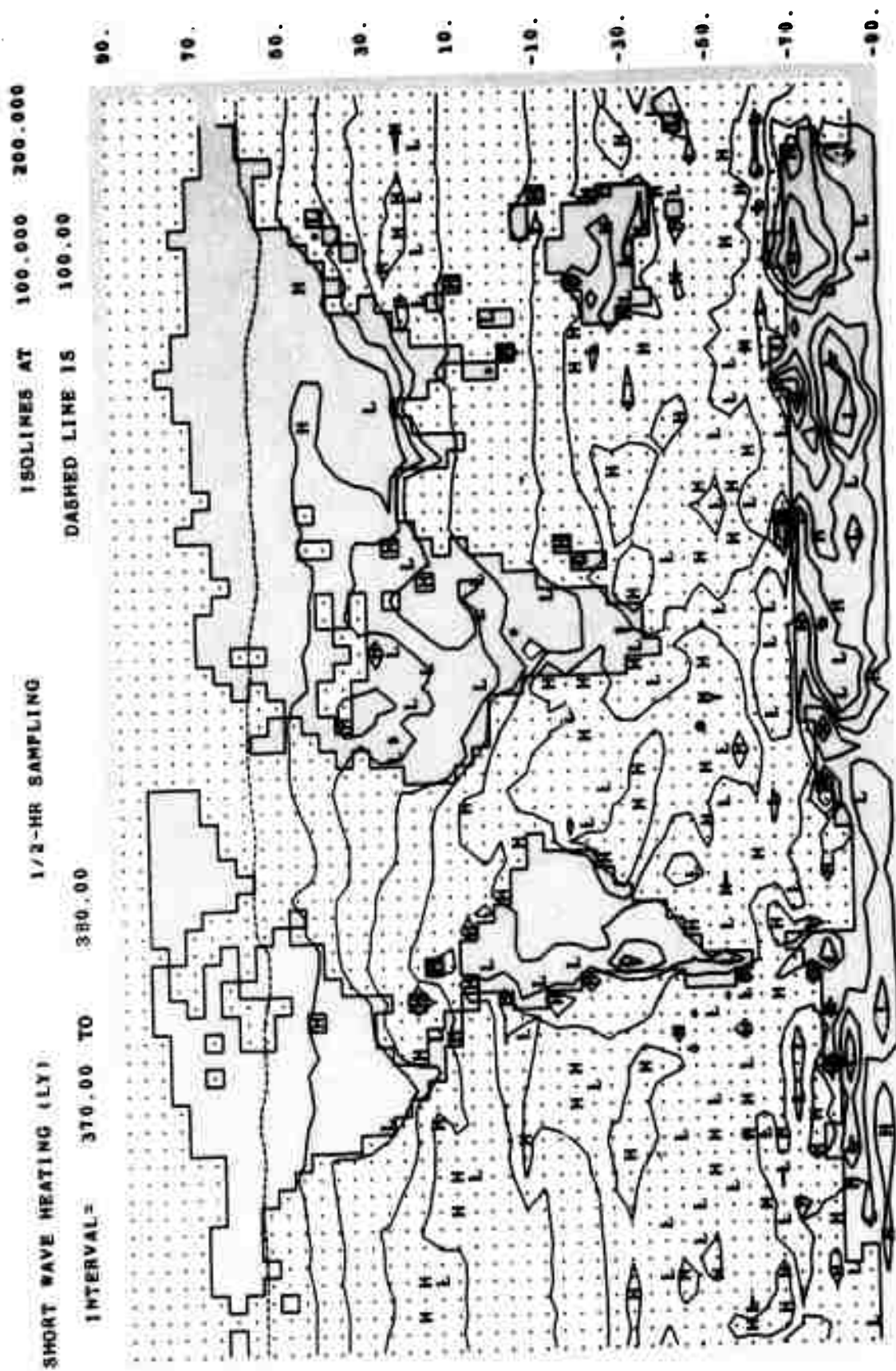


Fig. A2 -- Same as Fig. A1, but for a sampling every 1/2 hr (the program's frequency of radiation calculation).

When sampled every 12 hr (not shown), this sampling error appears as a 180° longitude harmonic of larger amplitude, and in the case of 24-hr sampling, there is no short-wave absorption at all over those parts of the earth that are (always) in darkness at sampling time. To minimize this sampling error, the product of the sampling interval and the angular rotation rate of the earth (15° hr^{-1}) should *not* be an integral multiple of the longitudinal grid size (5°). Preferably, the heating rate due to solar radiation absorption should be accumulated each time it is computed in the program. In Fig. A1 the anomalously large short-wave heating rates over Antarctica are due to the ice albedo error noted earlier (see Figs. 6 and 7). On the global average, the 6-hr and 1/2-hr sampling give nearly the same average heating rates due to short-wave absorption: 92.5 and 92.3 ly day^{-1} , respectively.

Of all the quantities examined, the latent heating $C_1 + C_3$ in Eq. (16) due to the parameterized convective condensation is the most sensitive to sampling frequency. Figures A3 and A4 show the average convective precipitation rate, P_c , as determined by both 6-hr and 1/2-hr sampling (over the selected 10-day period), to which the convective latent heating rate is proportional [see Eq. (22)]. In the case of an accurate accumulation of all convective condensation (1/2-hr sampling), there is a clear pattern to the average convective precipitation rate over the tropical oceans; maxima occur at approximately 20°N and 15°S , with secondary maxima over the midlatitude oceans. In the case of 6-hr sampling, the distribution over the tropical oceans becomes cellular and confused. This is due to the tendency of the simulated convective precipitation to occur at isolated points (or clusters of points) for short periods of time, usually much less than 6 hr. Such instantaneous condensation rates should not be applied to periods longer than those characteristic of the convection itself, which is here of the order of 1 hr. Sampling as infrequently as every 6 hr may also fail to adequately portray the diurnal nature of convection over the continents during daytime.

This error is also noticeable in terms of the zonally averaged distribution shown in Fig. A5. In the lower latitudes there is a

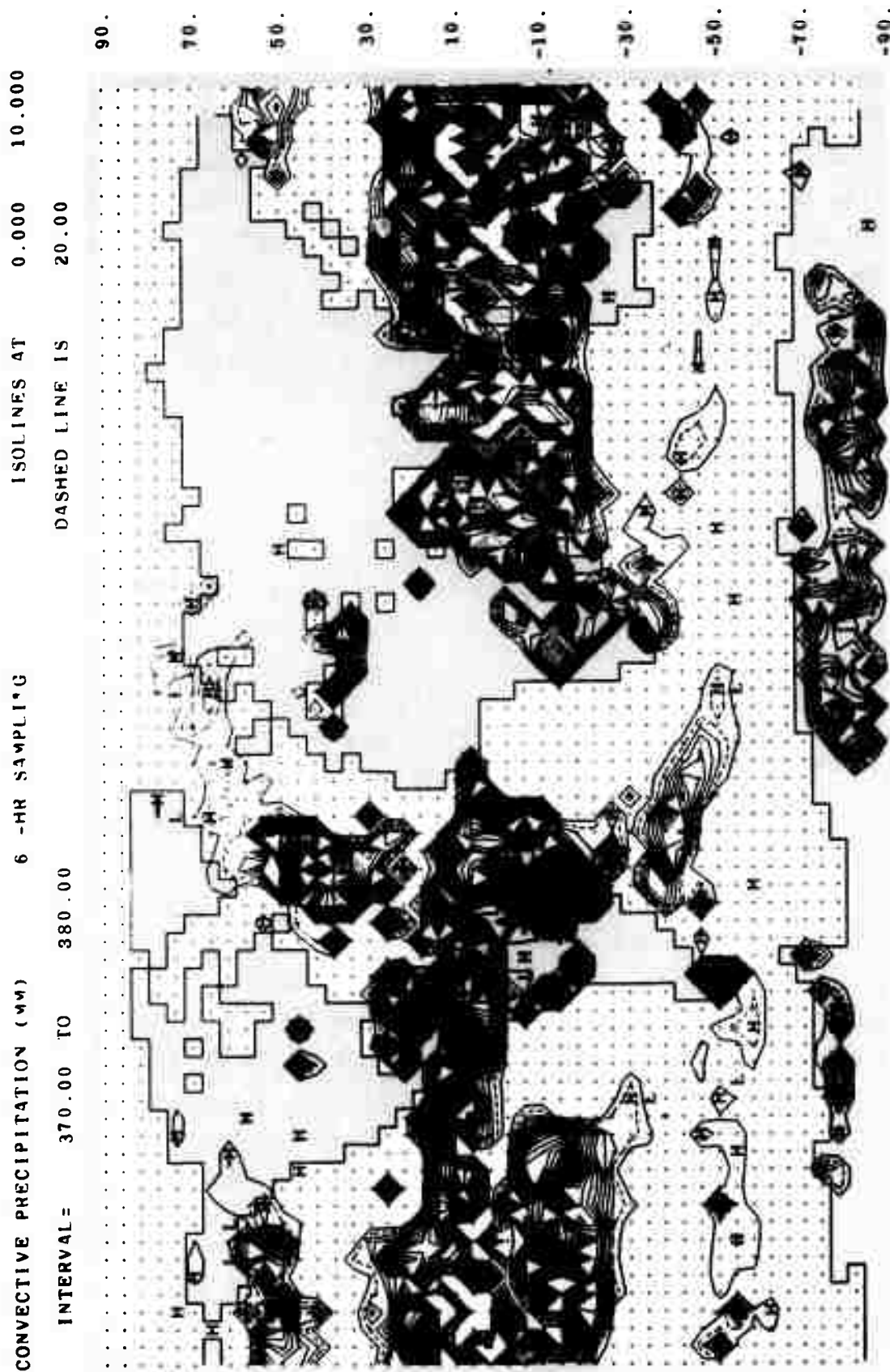


Fig. A3 -- The average rate of convective precipitation during 10 days of a January simulation, as given by sampling every 6 hr. The isolines are at intervals of 10 mm day⁻¹, with the 20 mm day⁻¹ isoline dashed.

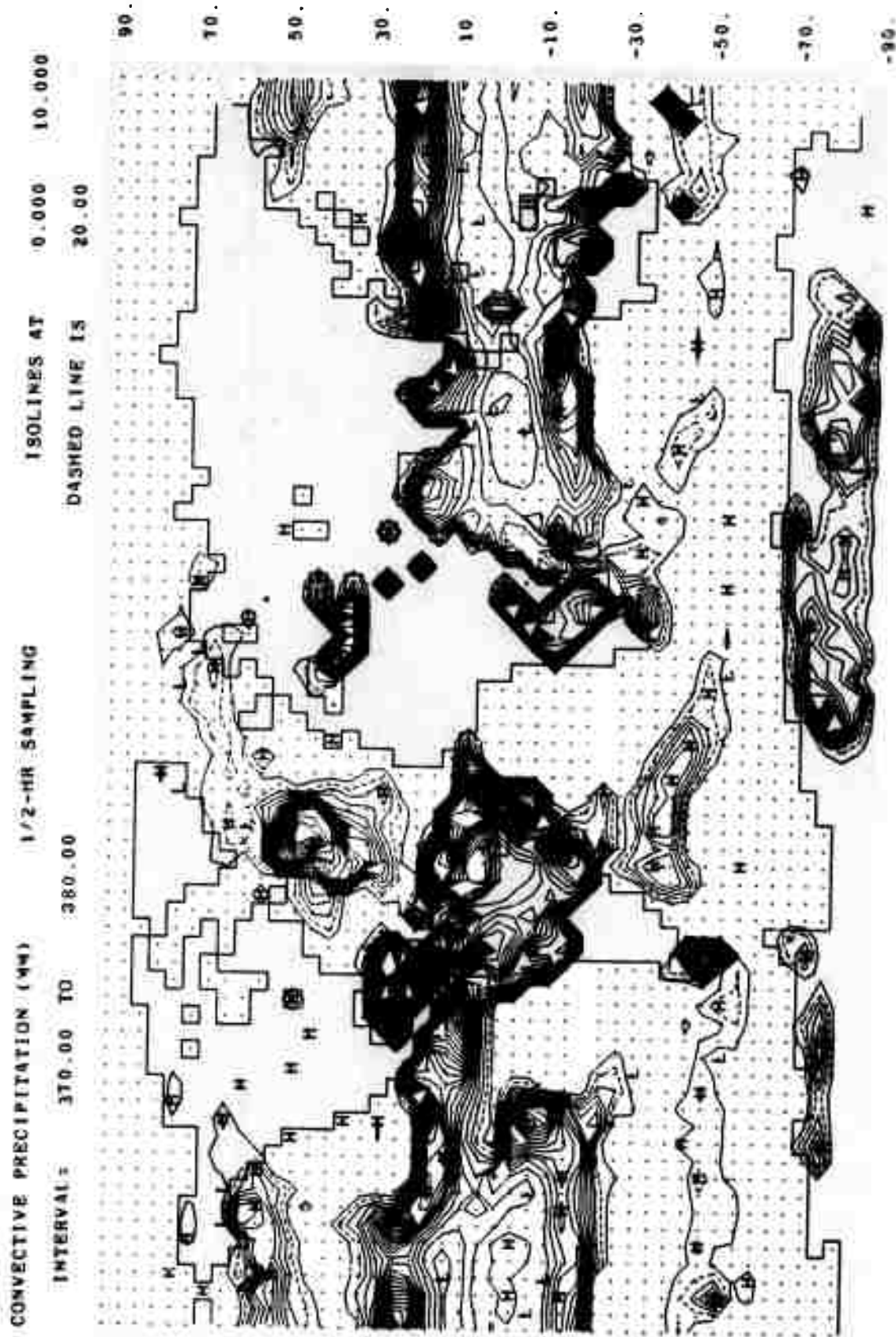


Fig. A4 -- Same as Fig. A3, but for a sampling every 1/2 hr (the program's frequency of precipitation calculation).

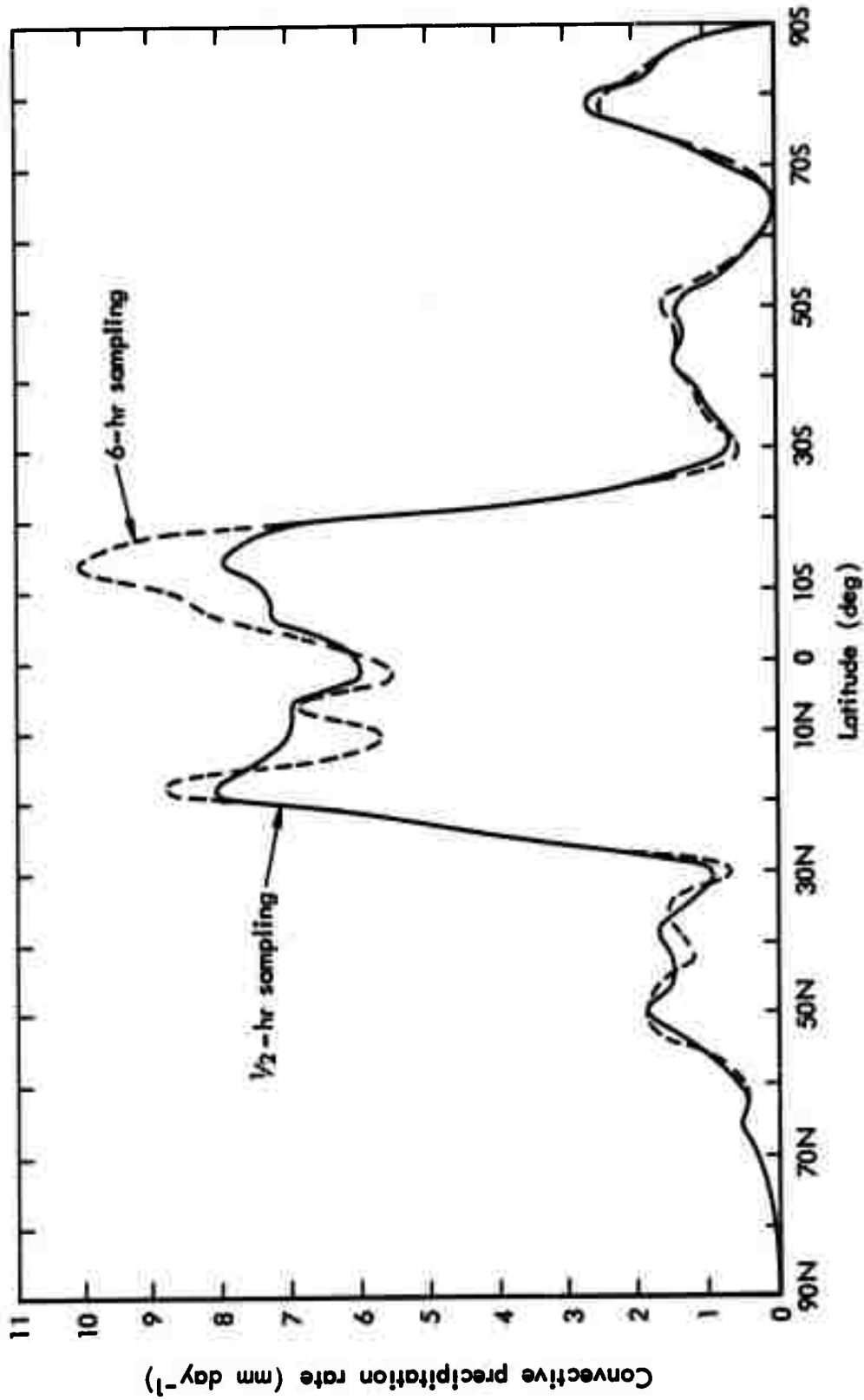


Fig. A5 -- The latitudinal distribution of the zonal average of the convective precipitation rate during 10 days of a January simulation. The solid curve is that given by $\frac{1}{2}$ -hr sampling (the program's frequency of precipitation calculation), and the dashed curve that given by 6-hr sampling.

sampling error of the order of 25 percent for the tropical convective rainfall, although on the global average, the 6-hr and 1/2-hr sampling cases give nearly the same average convective precipitation rate (3.52 and 3.48 mm day⁻¹, respectively). For both sampling intervals in Fig. A2 there is seen to be considerable convective precipitation over Antarctica; this is due to the model's inadvertent albedo error for ice, as previously discussed in connection with Figs. 6 and 10 (see also Fig. A5).

Although it shows no appreciable sampling error as noted earlier, the distribution of the precipitation rate $(PREC)L\pi/2g$ due to large-scale condensation is shown in Fig. A6 as determined from 1/2-hr accumulations. This precipitation is almost exclusively a middle- and high-latitude process, and shows maxima generally in the western portions of the midlatitude oceans. When added to the convective precipitation of Fig. A4 (1/2-hr case), this distribution gives the total precipitation rate.

Due mainly to the sampling sensitivity of the simulated convection (and the associated latent heating and convective precipitation), both the total heating rate \mathcal{K} and the net rate of moisture addition $E - P$ show a variation with sampling frequency. If these rates are constructed from data every 6 hr (instead of data from every 1/2 hr, as in Figs. 3 and 4), a distortion in low latitudes similar to that seen in Fig. A4 occurs. To obtain an accurate portrayal of the average total-heating and moisture-addition rates, it is apparently necessary to use the data from *each* step of the calculated convective process.

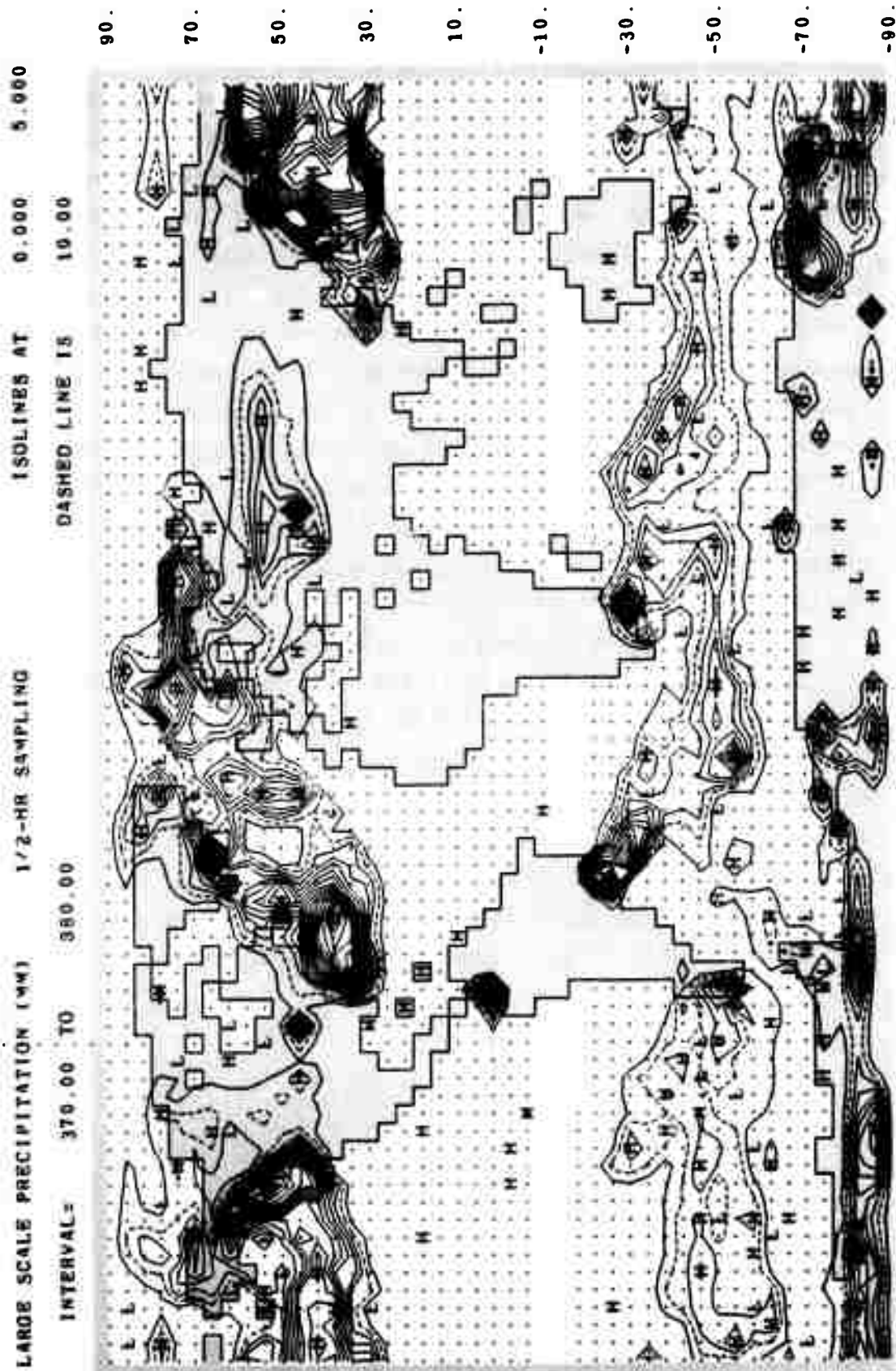


Fig. A6 --- Same as Fig. A1, except for the average large-scale precipitation rate as given by 1/2-hr sampling. The isolines are at 5 mm day⁻¹ intervals, with the 10 mm day⁻¹ isoline dashed. Note that here the isoline interval is half that used in Figs. A2 and A3.

REFERENCES

- Budyko, M. I., *Atlas of the Heat Balance of the Earth*, Gidrometeorizdat, Moscow, USSR, 1963, 69 pp.
- Cressman, G. P., "Improved Terrain Effects in Barotropic Forecasts," *Monthly Weather Review*, Vol. 88, No. 9-12, September-December 1960, pp. 327-342.
- Ellsaesser, H. W., "A Climatology of Epsilon (Atmospheric Dissipation)," *Monthly Weather Review*, Vol. 97, No. 6, June 1969, pp. 415-423.
- Gates, W. L., *The January Global Climate Simulated by the Two-Level Mintz-Arakawa Model: A Comparison with Observation*, R-1005-ARPA, The Rand Corporation, Santa Monica, Calif., 1972 (in process).
- Gates, W. L., Batten, E. S., Kahle, A. B., and Nelson, A. B., *A Documentation of the Mintz-Arakawa Two-Level Atmospheric General Circulation Model*, R-877-ARPA, The Rand Corporation, Santa Monica, Calif., 1971, 408 pp.
- Hellerman, S., "An Updated Estimate of the Wind Stress on the World Ocean," *Monthly Weather Review*, Vol. 95, No. 9, September 1967, pp. 607-626.
- Jacobs, W. C., "The Energy Exchange Between Sea and Atmosphere and Some of Its Consequences," *Bulletin of the Scripps Institute of Oceanography*, University of California, Vol. 6, 1951, pp. 27-122.
- London, J., *A Study of the Atmospheric Heat Balance*, Final Report, Contract AF19(122)-165, Department of Meteorology and Oceanography, New York University, 1957, 99 pp.
- Lvovitch, M. I., and Ovtchinnikov, S. P., *Physical-Geographical Atlas of the World*, Academy of Sciences, USSR, and Department of Geodesy and Cartography, State Geodetic Commission, Moscow, 1964, 298 pp.
- Möller, F., "Vierteljahrskarten des Niederschlags für die Ganze Erde," *Petermann's Geographische Mitteilungen*, Vol. 95, No. 1, 1951, pp. 1-7.
- Newell, R. E., Vincent, D. G., Dopplick, T. G., Ferruzza, D., and Kidson, J. W., "The Energy Balance of the Global Atmosphere," *The Global Circulation of the Atmosphere*, Royal Meteorological Society, London, 1970, pp. 42-90.
- Sasamori, T., London, J., and Hoyt, D. V., *Radiation Budget of the Southern Hemisphere*, NCAR Manuscript 71-100, National Center for Atmospheric Research, Boulder, Colorado, 1971, 49 pp.
- Schutz, C., and Gates, W. L., *Global Climatic Data for Surface, 800 mb, 400 mb: January*, R-915-ARPA, The Rand Corporation, Santa Monica, Calif., 1971, 173 pp.